



ELSEVIER

Available online at www.sciencedirect.com

SCIENCE @ DIRECT®

Solar Energy Materials
& Solar Cells

Solar Energy Materials & Solar Cells 78 (2003) 181–233

www.elsevier.com/locate/solmat

Photo- and electro-luminescence of a-Si:H and mixed-phase alloys

Daxing Han*, Keda Wang

*Department of Physics & Astronomy, University of North Carolina at Chapel Hill, Chapel Hill,
NC 27599-3255, USA*

Abstract

In this paper, we review recent work on photoluminescence in the transition materials from hydrogenated amorphous silicon (a-Si:H) to microcrystalline silicon ($\mu\text{c-Si:H}$) and silicon-germanium alloy (a-SiGe:H). Also, the electroluminescence is reviewed as transport-controlled recombination. We focus on the new materials such as hydrogen-diluted a-Si:H, a-Si:H prepared by hot-wire chemical vapor deposition, high-growth rate films, and the new findings concerning the electronic structure in relation to the material microstructures and to the solar cell performance such as open voltage (V_{oc}).

© 2003 Published by Elsevier Science B.V.

Keywords: Photoluminescence; Electroluminescence

1. Introduction

PL has been well studied to explore the recombination processes and electronic properties of localized states in hydrogenated amorphous silicon (a-Si:H) [1–4]. The large density of the localized tail states, especially of the valence band tail states, is the major influential factor in the PL processes in a-Si:H. Fig. 1 shows the schematic diagram of the PL processes that comprise photo-excitation of electron–hole pairs, carrier thermalization and recombination. Three mechanisms of carrier thermalization apply to a-Si:H: (a) rapid thermalization in extended states is completed in less than $<10^{-12}$ s; (b) thermalization by tunneling between localized states at low temperatures is described by hopping down [5]; and (c) thermalization by multiple trapping mechanism dominates above 50–100 K [6,7]. The recombination occurs after the carriers are trapped into the band tail states. There are two competing

*Corresponding author. Tel.: +1-919-962-5002; fax: +1-919-962-0480.

E-mail address: daxing@physics.unc.edu (D. Han).

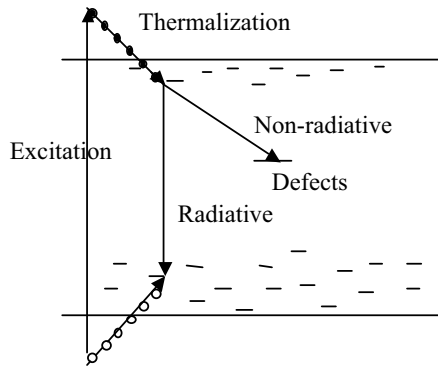


Fig. 1. Schematic diagram of the PL processes.

recombination channels, i.e. the radiative- and non-radiative recombination. The former involves the conversion of excitation energy into photons, the latter the conversion of the excitation energy into phonons. Photoluminescence (PL) is a measure of the photon emission via radiative recombination. The dominant recombination mechanism between band tail states is radiative transitions and the dominant recombination mechanism from the band edge to defect states is non-radiative transitions. In general, the radiative transition efficiency η can be described by

$$\eta = P_r / (P_r + P_{nr}) = 1 / (1 + P_{nr} / P_r), \quad (1.1)$$

where P_r and P_{nr} are the probability for radiative- and non-radiative transition, respectively. When the density of defects increases, P_{nr} increases and P_r decreases, and then η decreases. The radiative tunneling probability between localized electrons and holes that are spatially separated by a distance R can be written as

$$P_r = P_0 \exp(-2R/R_0) \text{ or when } R > R_0, \quad (1.2)$$

$$\tau_r = \tau_0 \exp(2R/R_0) \text{ when } R > R_0, \quad (1.3)$$

where R_0 is the localization length, the prefactor τ_0 is about 10^{-8} s and τ_r is the average carrier radiative-recombination lifetime. The absolute luminescence efficiency in device-quality a-Si:H samples is in the range of 0.3–1 at low temperatures of $T < 50$ K. The lineshape of PL spectrum from a-Si:H is characterized by a main band peaked at ~ 1.4 eV with full-width at half-maximum (FWHM) of 0.25–0.3 eV and a defect band peaked at ~ 0.9 eV. The PL main band dominates at low temperatures and both its intensity and peak energy position decrease as temperature increases due to carrier thermalization in the band tail states. The PL defect band shows a weak temperature dependence, and it is several orders of magnitude weaker than the main band at low temperatures. Thermal excitation from band tail states to the mobility edge becomes significant above 100 K and enhances the recombination via defects. One can find a complete description of PL in a-Si:H in Ref. [1] in which a thermalization model with an exponential band tail density of states ($\exp[-E/kT_0]$) is used to explain the features of the PL. The temperature

configuration coordinate diagram to describe these energies [1]. The energies of the ground state, $E_g(q)$, and excited state, $E_x(q)$, can be described in terms of the configuration q by

$$E_g(q) = Aq^2, \quad (1.6)$$

$$E_e(q) = E^* + Aq^2 - Bq, \quad (1.7)$$

where A is the strength of the network vibrations and the equilibrium state is at $q = 0$, and B is the linear deformation potential representing the strength of the electron–phonon interaction. The excited state has a minimum energy $E_e(q) = E^* - W$, where the relaxation energy, $W = B^2/4A$. The optical absorption measurements measure the transition between the ground state and the non-relaxed excited state, so the energy is $E_c + W$. The PL measures the photon emission energy $E_c - W$. The thermal excitation energy is E_c . The lattice relaxation energy W is about 0.2 eV. The difference between the absorption and the emission energy is the Stokes shift, $2W$ [1].

2. Instrumentation and techniques

The experimental layout for electroluminescence (EL) is shown in Fig. 3. A vacuum chamber is used to mount the sample. Most luminescence data were taken in the temperature range of 80–300 K using a MMR micro-refrigerator with a K-77 temperature controller. The luminescence signal is dispersed by a grating monochromator and then collected by a liquid-nitrogen-cooled Ge detector that is connected to a lock-in amplifier. The response curve of the detector and the system optics are calibrated with a linear response detector. For EL measurements, the applied voltage is obtained from a programmable pulse generator. 10 Hz repetition rate with 10 ms pulse width are typically used. We varied the forward bias current

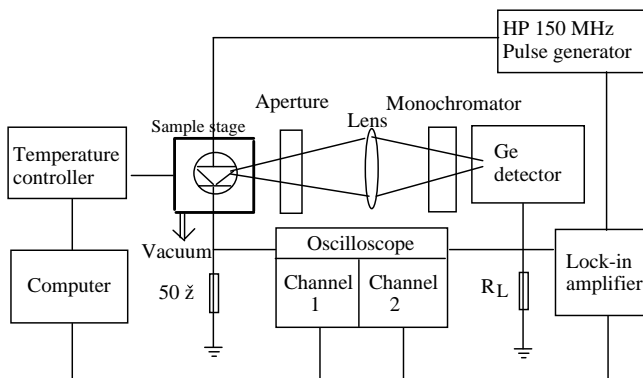


Fig. 3. EL experimental layout.

density between 10^{-4} and 10^2 mA/cm². The contribution of thermal radiation to the signal is less than 2% of the total signal [8]. The EL efficiency temperature dependence is measured under constant voltage conditions. The PL system is similar except that the excitation source is a laser light instead of the pulse generator and a light chopper at a frequency of 17 Hz is connected to the lock-in amplifier as a reference without using the oscilloscope.

The absolute intensity of luminescence is difficult to determine. The relative intensity is meaningful for studying a group of samples if one carefully keeps the same optical arrangement and the same sample configuration. In order to obtain comparable luminescence data, the film must be deposited on textured-surface substrate to avoid both the interference fringes and the effect of the internal reflection of the luminescence in the film. The PL measurements can be done on either thin film or device structures; the EL under double injection can be done on p-i-n or n-i-p diode structures. Several types of in-situ measurements are useful to gain insight into device physics such as in situ PL-EL and PL- V_{oc} measurements, as well as in situ light soaking.

The constant photoconductivity method (CPM) is used to measure the optical absorption spectrum. Infrared (IR) absorption is used to measure the hydrogen content and its bonding configuration and Raman scattering to measure the bonding structure of the silicon matrix.

3. Atomic- and electronic structures in transition materials from amorphous to microcrystalline silicon thin films prepared by HW-CVD

The transition films from a-Si:H to microcrystalline silicon (μ c-Si:H) have attracted a great deal of attention because the most stable, high-performance a-Si:H solar cells were prepared at a hydrogen-to-disilane dilution ratio just below the onset of microcrystallinity [9]. On the other hand, increasing the grain size and reducing the defects are important issues for thin film c-Si and their device applications [10]. μ c-Si:H films can be directly deposited at substrate temperatures (T_s) of 200–300°C in a plasma-enhanced chemical vapor deposition (PE-CVD) system with high hydrogen dilution ratio, but the deposition rate is very low. Many efforts have been made to increase the deposition rate such as using very high frequency plasma CVD [11] and using a microwave-based technique [12]. A deposition rate of ~ 10 Å/s is standard for the hot-wire (HW-CVD) technique [13], and it does not require high hydrogen dilution ratios to make the phase transition [2]. The crystallinity of μ c-Si:H films has been determined using Raman, X-ray diffraction (XRD), and high-resolution transmission electron microscopy [9,10]. More recently, the electronic density of states (DOS) of the transition films has been studied by PL spectroscopy, optical absorption spectra using CPM, and photocapacitance spectra [2,3,9]. In addition to the difference in growth rate, some new features of H microstructure in PE-CVD transition films have been reported [14,15]. The authors reported an enhanced hydrogen concentration in the a- to μ c-Si:H transition zone; and when the film is in the μ c-Si:H regime, the absorption peaks are much narrower around 626,

900 and 2101 cm⁻¹ than the typical peaks at 640, 840, 880, 2000, and 2090 cm⁻¹ in a-Si:H [14]. A systematical study of the transition materials from a- to μc-Si:H prepared by HW-CVD is presented next.

3.1. Sample and experimental

Intrinsic a-S:H films were deposited by HW-CVD on c-Si substrates for IR, on rough-surface Corning 1737 glass for PL and Raman, on smooth surface Corning 1737 glass for transmission spectroscopy (TRS), and CPM studies. Group I films were deposited at the same substrate temperature, $T_s=250^{\circ}\text{C}$, with varied hydrogen dilution ratio, $R=H_2:\text{SiH}_4$, from 0 to 10. Group II films were deposited at the same $R=3$ with varied substrate temperature, T_s , from 150°C to 550°C . In addition, a reference sample was deposited at 560°C with pure silane. The film preparation conditions and parameters are listed in Table 1. Group III films were deposited at $\sim 240^{\circ}\text{C}$ with R varying from 0, to 20 using a separate deposition system. The characteristics are listed in Table 2.

Raman spectra were measured using an *XY* triple spectrograph equipped with a LN2-cooled CCD camera. The data were taken at room temperature using the 514.5 nm line of an argon-ion laser. The power of the laser was kept below the level that would thermally induce crystallization. IR spectra were measured at room temperature by a commercial FTIR spectrometer. The details of IR measurements can be found elsewhere [16]. For PL measurements, a 5-mW HeNe laser with a bandpass filter was used for PL excitation. The penetration depth of the 632.8 nm light in a-Si:H was $\sim 1\mu\text{m}$ which is greater than the sample thickness. Between consecutive measurements, the sample was kept at the same position and the experimental error was $<10\text{ meV}$ in the experimental range of photon energy. The

Table 1
Preparation conditions and parameters of the transition films prepared by HW-CVD.

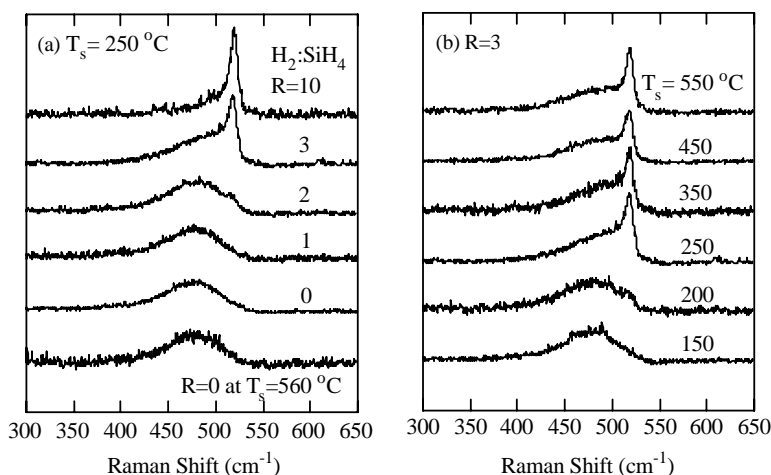
Sample	ID	T_s ($^{\circ}\text{C}$)	R H_2/SiH_4	Thickness (μm)	Dep. rate ($\text{\AA}/\text{s}$)	C_H (at%)	E_{opt} (eV)	n	c-Si volume fraction (%)
Group I	H955	250	0	0.8	4.7	12.6	1.76	3.55	0
	H946	250	1	0.5	4.7	10.9	1.80	3.60	0
	H948	250	2	0.7	4.7	8.9	1.78	3.45	2
	H947	250	3	0.7	4.7	6.2	1.82	3.36	43
	H945	250	10	1.0	3.9	4.1	1.77	3.36	82
Group II	H954	150	3	0.7	4.3	9.7	1.81	—	0
	H951	200	3	0.7	4.7	8.3	1.80	3.4	3
	H947	250	3	0.7	4.6	6.2	1.81	3.36	41
	H950	350	3	0.7	4.7	5.5	1.78	3.41	44
	H952	450	3	0.7	4.4	3.8	1.74	3.53	36
	H953	550	3	0.7	4.4	3.2	1.72	3.52	37
Ref.	H949	560	0	1.0	9.0	7.1	1.72	—	0

C_H , E_{opt} and n represent the hydrogen content, the Tauc optical gap [17], and the refraction index.

Table 2

Structure and parameters of group III films with varied H-dilution ratio

Sample ID	H ₂ /SiH ₄ (R)	Thickness (μm)	Dep. rate (Å/s)	C _H (at%)	X _c (%)	Spectral lineshape of optical absorption
T516	1	4.1	17.2	13.3	0	a-Si like + 1.2 eV band
T534	2	3.0	12.5	10.9	0	a-Si like + 1.2 eV band
T532	3	1.7	7.08	4.0	68	Poly Si like
T529	4	2.4	8.0	4.2	81	Poly Si like
T528	5	2.1	7.0	3.1	83	Poly Si like
T518	10	1.4	3.9	4.7	89	Poly Si like
T519	20	1.1	2.3	3.9	92	Poly Si like

C_H is hydrogen content and X_c is c-Si volume fraction from XRD.Fig. 4. Raman shifts from groups I and II films with (a) different hydrogen dilution ratio, R , and (b) varied substrate temperature, T_s . The Raman spectrum from the reference film is shown at the bottom of (a).

optical absorption spectra were studied by using CPM combined with TRS at room temperature.

3.2. Results and discussion

3.2.1. Raman spectrum

Typically, the Raman transverse optic (TO) mode peaks at 480 cm^{-1} with a FWHM of $\sim 70\text{ cm}^{-1}$ for device-quality a-Si:H films. The Raman lineshape does not change with microvoid density in high growth rate films [4]. Figs. 4a and b show the Raman results from groups I and II films, respectively. The Raman result from the reference film is shown at the bottom of Fig. 4a. Concerning the hydrogen dilution dependence, when $R \leq 1$, the film remains in the amorphous phase characterized by the broadband centered at 480 cm^{-1} . At $R = 2$, one can see an emergence of the band

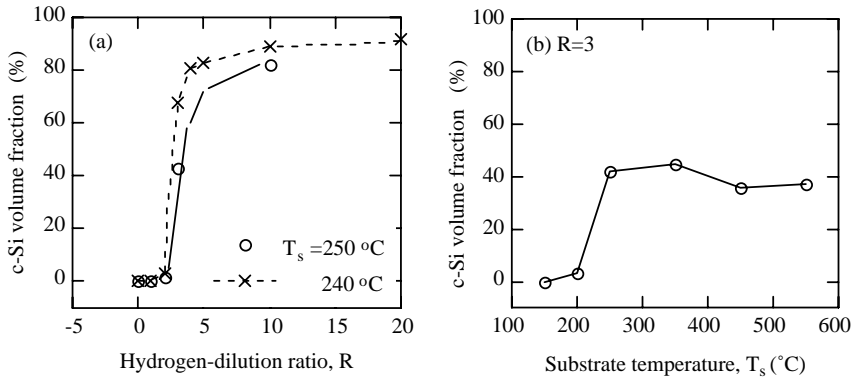


Fig. 5. The correlation of c-Si volume fraction with (a) hydrogen dilution ratio, R at $T_s = 240^\circ\text{C}$ (\times) and 250°C (\circ), and (b) substrate temperature T_s at $R = 3$.

at 520 cm^{-1} . The 520 cm^{-1} band grows as R is increased. Finally, the 520 cm^{-1} band dominates at $R = 10$. Fig. 4b shows the substrate temperature dependence at $R = 3$. When $T_s < 200^\circ\text{C}$, the film remains fully amorphous; when $T_s = 200^\circ\text{C}$, there is an emergence of the band at 520 cm^{-1} . When $T_s \geq 250^\circ\text{C}$, a saturated height of the narrow band at 520 cm^{-1} is observed after the onset of microcrystallinity. Unlike the case of increasing R , there is no gradual increase of the 520 cm^{-1} band as T_s is increased. The bottom curve of Fig. 4a shows that the film deposited at 560°C at $R = 0$ remains amorphous.

$\mu\text{c-Si}$ materials consist of the a-Si matrix, the c-Si grains and the grain boundaries (g.b.). For the best curve fitting we used three components: the narrow crystalline band at 520 cm^{-1} , a Gaussian function peaked at 480 cm^{-1} with a FWHM 72 cm^{-1} , and a Gaussian function peaked at $498\text{--}505\text{ cm}^{-1}$ which is associated with bond dilation at g.b. Notice, for these three groups of films, the a-Si:H band was at the same energy position with the same FWHM. This implies that the growth of the c-Si grains does not change the local Si-Si bonding structure of the a-Si:H matrix. The microcrystalline and g.b. volume fractions, X_c , and X_{gb} were estimated from $X_c = (I_c + I_{gb}) / [I_c + I_{gb} + y(L)I_a]$, and $X_{gb} = I_{gb} / [I_c + I_{gb} + y(L)I_a]$ where I_c , I_a , and I_{gb} are integrated intensities of the crystalline, amorphous, and intermediate peaks, respectively, and $y = 0.9$ was used [2]. The results are plotted in Figs. 5a and b. One can see a rapid increase of the c-Si volume fraction at the threshold hydrogen dilution ratio $R = 2$ in Fig. 5a for both groups I and III, and a threshold substrate temperature $T_s = 200^\circ\text{C}$ in Fig. 5b. The curves in Fig. 5a indicate that the c-Si volume fraction can be as large as $> 90\%$ at $R = 20$. On the other hand, the saturated curve in Fig. 5b indicates that, at fixed $R = 3$, the c-Si volume fraction reaches a maximum of $42 \pm 1\%$ at $250 \leq T_s \leq 300^\circ\text{C}$, then slightly decreases to 33% at $350 \leq T_s \leq 550^\circ\text{C}$.

3.2.2. IR absorption

Hydrogen plays a crucial role in determining the structural phase transition of a-Si:H. The question then arises as to what are the hydrogen distribution and local

bonding configuration in regard to the microcrystallinity. IR spectra were used to study the Si–H vibration absorption. Generally, IR spectra of a-Si:H consist of three absorption regions: at 630 cm^{-1} related to the SiH wag mode, a doublet at $850, 890\text{ cm}^{-1}$ related to SiH_2 bending modes, and the peaks at $2000\text{--}2090\text{ cm}^{-1}$ related to SiH stretch modes [16,18–20]. For groups I and II film, Figs. 6a–c show the IR spectra in the three frequency ranges of $550\text{--}750\text{ cm}^{-1}$, $750\text{--}1200\text{ cm}^{-1}$ and $1800\text{--}2200\text{ cm}^{-1}$ that cover the SiH wag mode, the SiH_2 bending mode, SiO modes, and the SiH and/or SiH_2 stretch modes. All the peaks in Fig. 6 were fitted using Gaussian functions and the integral intensity $I=\omega^{-1}\alpha(\omega)\delta\omega$ was calculated. Assuming the absorption strength, A , is a constant, the corresponding hydrogen concentrations, N_{630} , $N_{850,895}$, N_{2090} and N_{2000} , were calculated using $A_{630}=2.1\times 10^{19}\text{ cm}^{-2}$,

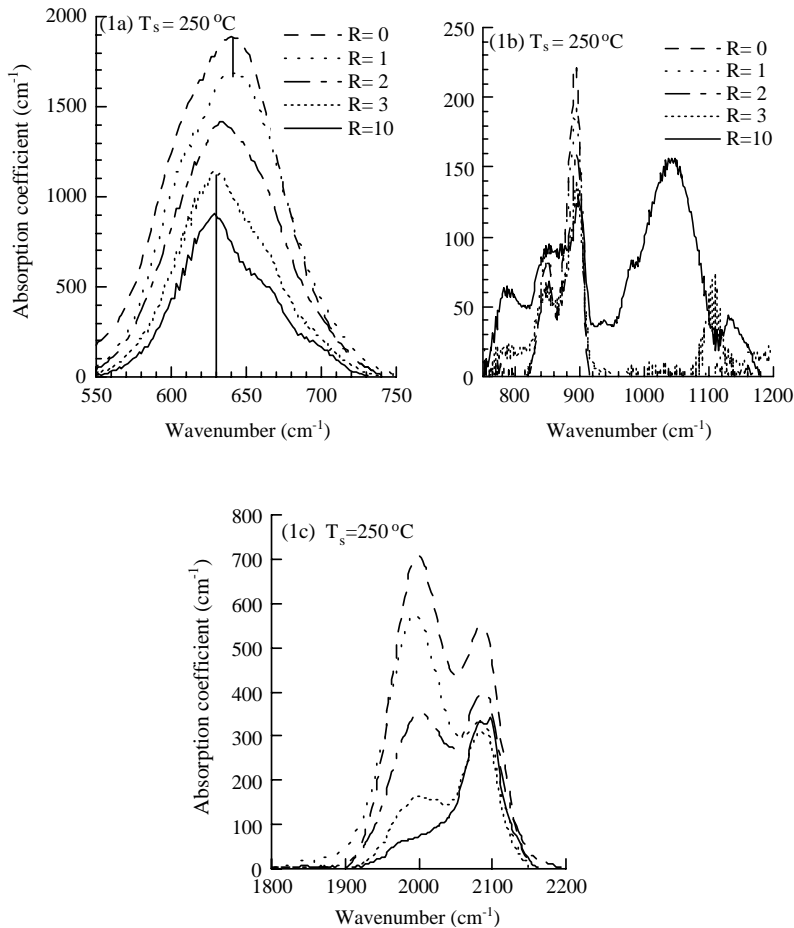


Fig. 6. The IR spectra in three frequency ranges of $550\text{--}750$, $750\text{--}1200$ and $1800\text{--}2200\text{ cm}^{-1}$ that cover the Si–H wag mode, the SiH_2 bending mode, Si–O modes, and the stretch modes (a–c) for group I and (A–C) for group II films. The values of R and T_s are indicated in the legend.

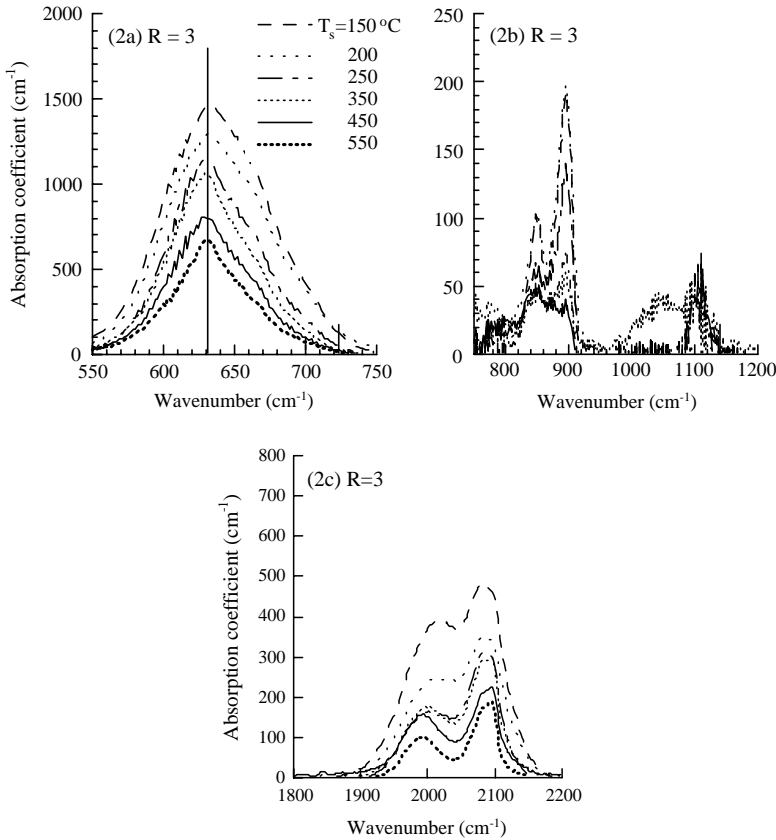


Fig. 6 (continued).

$A_{850,895} = 2 \times 10^{19} \text{ cm}^{-2}$, $A_{2090} = 2.2 \times 10^{20} \text{ cm}^{-2}$ and $A_{2000} = 9.0 \times 10^{19} \text{ cm}^{-2}$ [16,18]. The peak energy positions and the FWHM for the SiH wag and stretch modes as well as the percentage of the $850\text{--}895 \text{ cm}^{-1}$ mode concentration, $N_{850,895}/N_{630} = I_{850,895}/I_{630}$, and the percentage of the 2090 cm^{-1} mode absorption, $I_{2090}/(I_{2000} + I_{2090})$, are listed in Table 3. The hydrogen concentration is calculated by

$$C_H = N_{630}/N_{Si} = (A_{630}I_{630})/N_{Si}, \quad (3.1)$$

where $N_{Si} = 5 \times 10^{22} \text{ cm}^{-3}$ is used. Figs. 7a and b show the C_H (the solid circles) and the ratio of $I_{2090}/(I_{2000} + I_{2090})$ (the open circles) as a function of R and T_s . The big cross in Fig. 7b represents the reference film. In a previous work, Kroll et al. [14] observed a considerably enhanced hydrogen concentration in/near the a/ μ c-Si transition zone in PE-CVD films. They suggested that it is due to molecular hydrogen trapped in microvoids. Such an enhanced C_H zone has not been found in these HW-CVD films. Instead, the C_H decreases in two regimes of fast and slow in both group I and group II films. The turning points from the fast to slow regime are

Table 3

The energy peak position and the bandwidth of the Si–H vibration modes

Sample ID	T_s (°C)	R	Wag mode peak, FWHM (cm ⁻¹)		Stretch mode 1 peak, FWHM (cm ⁻¹)		Stretch mode 2 peak, FWHM (cm ⁻¹)		$I_{2090}/(I_{2000} + I_{2090})$ (%)	$N_{850,895}/N_H$ (%)
H955	250	0	640	89	2000	86	2085	62	32	3
H946	250	1	640	89	1995	94	2088	62	23	3
H948	250	2	635	87	2002	94	2088	62	38	3
H947	250	3	631	75	2005	94	2090	62	52	5
H945	250	10	631 ^a	68	2010	113	2088	62	68	5
H954	150	3	630	87	2000	112	2090	69	38	4
H951	200	3	630	87	2000	112	2092	69	42	5
H947	250	3	630	76	2005	95	2090	60	52	5
H950	350	3	630	69	2001	86	2088	55	50	3
H952	450	3	630	64	1995	86	2088	55	46	4
H953	550	3	630	57	1996	67	2088	45	50	5
H949	560	0	635	95	1996	86	2088	86	14	0.4

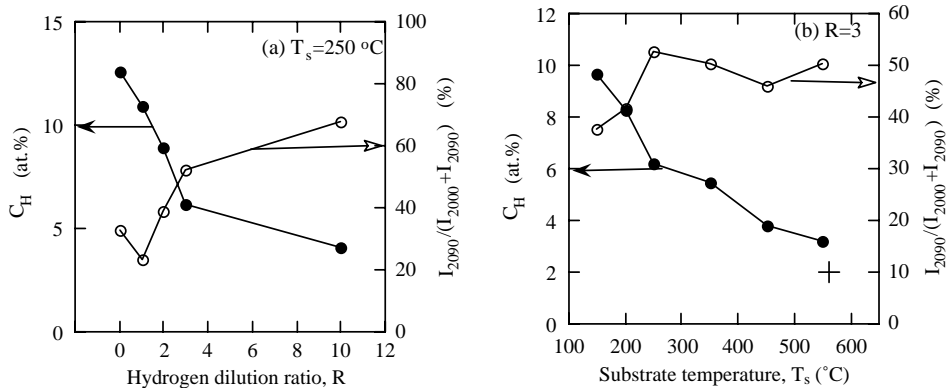
^aThere is a small shoulder at 670 cm⁻¹.

Fig. 7. The correlation of the hydrogen concentration, C_H (●), the relative intensity of the 2090 cm⁻¹ peak, $I_{2090}/(I_{2000} + I_{2090})$ (○), with (a) varied H-dilution ratio, R , and (b) varied substrate temperature, T_s . The big cross in (b) represents the reference film.

correlated with the onset of crystallinity. Based on the data from nuclear magnetic resonance (NMR) and gas effusion for mixed-phase materials, most hydrogen clusters are located in the g.b. [21–24]. When the material becomes $\mu\text{c-Si:H}$, the g.b. acts as a reservoir for hydrogen. This causes the slow decrease regime in total hydrogen content. On the other hand, the changes of the ratio $I_{2090}/(I_{2000} + I_{2090})$ totally follow the manner of microcrystallinity. In addition, the hydrogen concentration, $N_{2000} + N_{2090}$, shows exactly the same two regimes of fast and slow decreases as shown in Figs. 7a and b, and is about 5% less than that calculated from

the SiH wag mode, N_{630} . This is within the accuracy of the technique. So, the contribution from the SiH_2 stretch vibration to the 2090 cm^{-1} absorption is negligible and the 2090 cm^{-1} absorption is attributed to the stretch vibration of clustered SiH in the g.b. regions. The next question is whether the SiH bonds are sticking on the cone-shaped c-Si grain surfaces [25] or are just clustered in the g.b. regions. The latter is more likely because there are 32% and 14% of $I_{2090}/(I_{2000} + I_{2090})$ in the a-Si:H films without c-Si grains (see sample H955 and H949 with $R = 0$ in Table 3), and the changes of the relative intensity, $I_{2090}/(I_{2000} + I_{2090})$, correlate well with the g.b. volume fraction. More evidence supports the above arguments. The frequency range of $2085\text{--}2092\text{ cm}^{-1}$ is consistent with the SiH stretch frequencies of $2080\text{--}2098\text{ cm}^{-1}$ that were found in a-Si surfaces [26]; and the results of gas effusion compared to IR absorption show that the $850\text{--}890$ and 2100 cm^{-1} modes are both related to Si–H bonds in g.b. in $\mu\text{c-Si:H}$ films [21].

The peak energy and linewidth of the IR spectra are listed in Table 3. There is neither a red shift of the wag mode nor a narrowing of the FWHM with increasing of microcrystallinity as those reported in PE-CVD films [14,15]. The frequency of the SiH wag mode is located at $630\text{--}640\text{ cm}^{-1}$ regardless of whether the film structure is a-Si:H or $\mu\text{c-Si:H}$. In group I films, the FWHM of the wag mode decreases from 89 to 68 cm^{-1} as the crystallinity increases from 0 to $\sim 82\%$, whereas the FWHM of the 2000 cm^{-1} stretch mode increases from 86 to 113 cm^{-1} without a change of the FWHM in the 2090 cm^{-1} stretch mode. In group II films, the FWHM for both wag and stretch modes behave the same, i.e. they slightly decrease with an increase of crystallinity when $150^\circ\text{C} < T_s < 350^\circ\text{C}$, and rapidly decrease with an increase of the substrate temperature for $T_s > 350^\circ\text{C}$ without an increase of crystallinity. Hence, the main factor that accounts for the decrease in FWHM is the substrate temperature.

In these HW-CVD films, in addition to the doublet at $850\text{--}900\text{ cm}^{-1}$, the SiO related modes at 750 and $\sim 1000\text{--}1200\text{ cm}^{-1}$ [20] appear when the c-Si volume fraction is above $\sim 40\%$ as shown in the curves with $R = 3$ and 10 in Fig. 6b and with $T_s = 450^\circ\text{C}$ and 550°C in Fig. 6b. This is because of the fast oxidation in air due to the porous-like structure [27]. The porous-like structure is, perhaps, due to the high growth rate of c-Si grains, which leave the g.b. regions with much less mass density. Compared to PE-CVD a-Si:H, the HW films exhibit higher structural inhomogeneity and a larger percentage of clustered hydrogen [22,28]. It is reasonable that the structure becomes porous if the c-Si grains grow fast without the plasma etching out the weak bonds. In a recent work, Ferreira et al. [27] used a plasma-assisted HW-CVD technique and found no SiO vibration band present in their compact nanocrystalline silicon films.

3.2.3. Optical absorption spectra

The Tauc optical gap, E_{opt} , was deduced from the absorption spectrum between 1.7 and 3.0 eV [17]. The results are listed in Table 1. Figs. 8a and b show the optical absorption coefficient spectra, $\alpha(h\nu)$, obtained by using CPM and fitted by TRS for group III and II films, respectively. The typical absorption spectrum of c-Si is plotted in Fig. 8a for reference. The group II and group III films were deposited on smooth- and rough surface substrates, respectively. Hence, the curves in Fig. 8b with

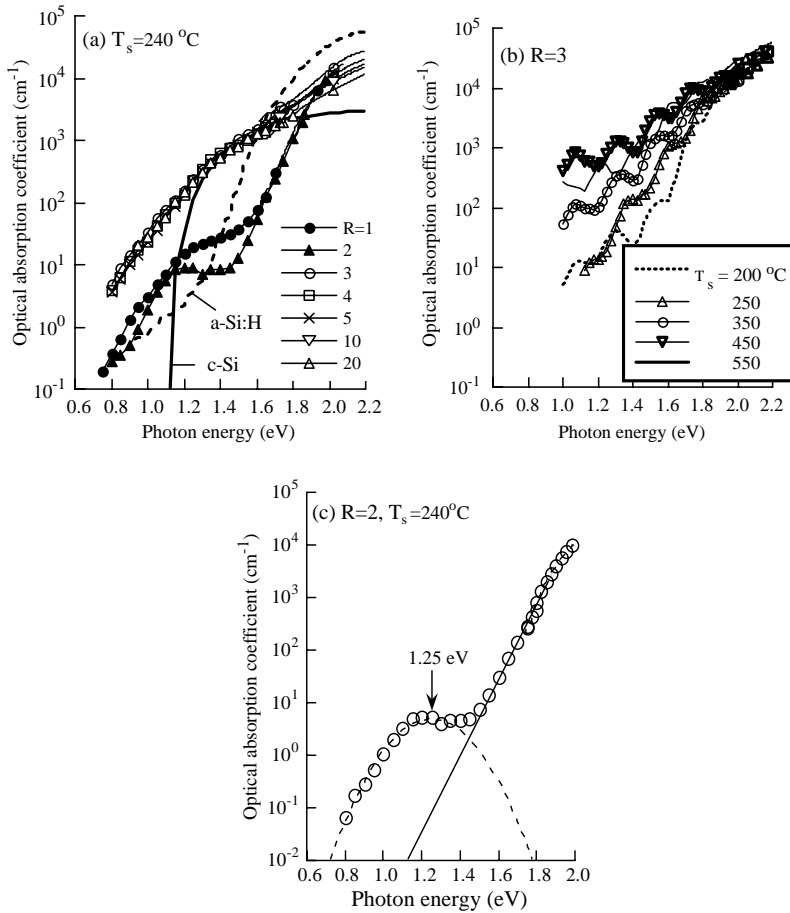


Fig. 8. Optical absorption spectra obtained by using CPM and fitted by TRS for (a) group I and (b) group II films. The values of R and T_s are indicated in the legend. The absorption spectra for c-Si are plotted in (a) for reference. (c) Gaussian function fit for the extra optical absorption peak for the film with $R = 2$ at $T_s = 240^\circ\text{C}$.

interference fringes and the curves in Fig. 8a without. The absorption is contributed by the transitions from three components: the a-Si:H matrix, the c-Si grains and the g.b. Fig. 8c shows the Gaussian function fits for the extra optical absorption peak from g.b. for the film with $R = 2$ (see Fig. 8a). The $\alpha(1.4\text{ eV})$ is as small as $\approx 1\text{ cm}^{-1}$ in a device-quality a-Si:H matrix [17]. In order to extract the DOS related to microcrystallinity, we plot the $\alpha(1.4\text{ eV})$ as a function of R , and T_s in Figs. 9a and b. The dotted and the solid lines indicate the c-Si volume fractions and the $\alpha(1.4\text{ eV})$, respectively. For the H-diluted films shown in Fig. 9a, the data of $\alpha(1.4\text{ eV})$ in logarithmic plot and c-Si volume fraction are clearly correlated. When R increases, the density of electronic states related to $\alpha(1.4\text{ eV})$ increases due to an increase of

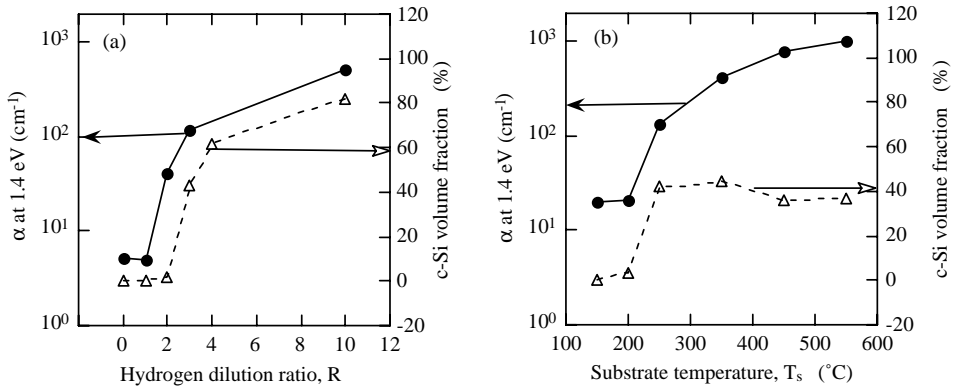


Fig. 9. Comparing the optical absorption coefficient at 1.4 eV (●) and the c-Si volume fraction (Δ) as a function of (a) R , and (b) T_s .

crystallinity. For the group II films shown in Fig. 9b, when $T_s > 250^\circ\text{C}$, the c-Si volume fraction does not increase but $\alpha(1.4\text{ eV})$ does. This indicates an increase of both the tail states and the defect states in the a-Si matrix at high deposition temperature [17] due to less hydrogen incorporation.

3.2.4. PL spectra at 80 K

The PL signal at low temperatures of $T < 100\text{ K}$ is dominated by radiative band tail-to-band tail transitions [1]. A low-energy band at $\sim 1.0\text{ eV}$ has been observed in $\mu\text{c-Si}$ films [2]. For group I and II films, the relative intensity of the PL spectra at 80 K is given in Figs. 10a and b. The bottom dotted line in Fig. 10a represents the PL spectrum from the reference film. The intensity of the PL is 100 times reduced for the films with $R = 0, 1$, and 2 films in Fig. 10a and 50 times reduced for the films with $T_s = 150^\circ\text{C}$ and 200°C in Fig. 10b. It means that the relative PL intensity is higher in group I films than in group II films. The PL intensity is especially low for the films with high $T_s = 450^\circ\text{C}$ and 550°C . This is due to the high density of non-radiative centers, in agreement with the optical absorption data in Figs. 9b. More radiative centers exist at the g.b. regions in the group I films. For the reference film, the relative PL efficiency is as high as the a-Si:H film deposited at 250°C except the peak energy is lower. Nevertheless, it is clear that the PL features also indicate a sudden change from amorphous to microcrystalline at the same thresholds of R and T_s . One observes that the low energy PL from g.b. becomes dominant and the PL total intensity decreases as either R or T_s increases.

3.3. The role of grain boundary in the properties of $\mu\text{c-Si:H}$

We observed that both the hydrogen bonding distribution and optoelectronic properties are well correlated to the material's crystallinity. This is mainly related to

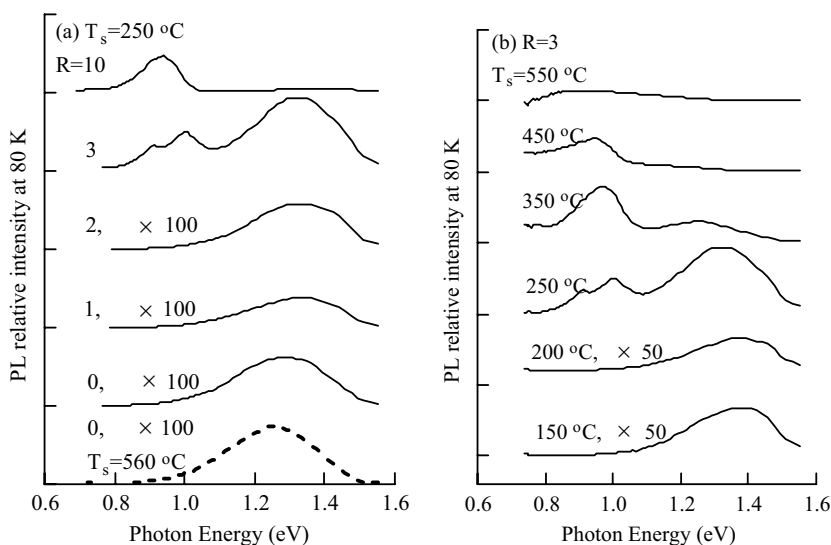


Fig. 10. Relative PL spectral intensity at 80 K for (a) group I and (b) group II films. The PL spectrum for the reference film is shown on the bottom of (a).

the formation of the grain boundaries. In summary

- (a) With an increase in either R or T_s , the hydrogen content, C_H , decreases in a fast and slow regime separated by the onset of microcrystallinity. We describe that this is due to the grain boundaries acting as a reservoir for hydrogen, which makes the decrease of total hydrogen content slow down.
- (b) The relative absorption of the 2090 cm^{-1} peak, $I_{2090}/(I_{2000} + I_{2090})$, but not the $850\text{--}890\text{ cm}^{-1}$ peak, increases with c-Si volume fraction. Therefore, we attribute the 2090 cm^{-1} peak to the SiH stretch vibration from the clustered SiH in the g.b. regions but not to silicon dihydride. Meanwhile, the frequency of the wag mode remains unchanged at $630\text{--}640\text{ cm}^{-1}$ no matter whether the SiH oscillator is clustered or distributed.
- (c) The density of electronic states was studied by optical absorption and PL spectra. The optical absorption spectra of $\mu\text{c-Si:H}$ films indicate that the electronic states in the g.b. region result in an absorption band that peaks at $\sim 1.25\text{ eV}$. If the Stokes shift is about 0.25 eV , then the $\sim 1.0\text{ eV}$ PL band originates from the same states.
- (d) The absorption coefficient α at 1.4 eV is used to describe the DOS related to microcrystallinity. The same threshold of the material's crystallinity is also visible in the increase of $\alpha(1.4\text{ eV})$, in its relevant PL (1.0 eV) band, and in the position of Fermi level. We conclude that the increase of crystallinity results in an increase of the low-energy electronic density of states including both radiative and non-radiative centers.

- (e) The low-energy PL band from $\mu\text{c-Si:H}$ films was carefully studied. The decreases of the PL intensity and peak energy follow the model of carrier thermalization in an exponential band tail.

We conclude that controlling hydrogen dilution is the key factor to depositing device-quality $\mu\text{c-Si:H}$ films. Deposition at $T_s=240\text{--}250^\circ\text{C}$ with different R produces films with either the lowest defect density or the highest volume fraction of crystallinity [2,3]. However, a high growth rate results in a relatively high density of microvoids [4]. The porous structure of highly microcrystallized films causes an oxidation problem that can be solved [27].

3.4. Structural inhomogeneity of the transition films along the growth direction

The inhomogeneous growth of the c-Si grains is studied by Raman and PL on group III films. The penetration depth of 514.5 nm light is 60 and 200 nm in the case of a-Si:H and $\mu\text{c-Si}$, respectively. Thus, the 514.5 nm laser probes only a thin surface layer. Figs. 11a and b show the Raman spectra at room temperature for front- and back-excitation of the same group of films. In Fig. 11b one can see that the interface layers near the substrates remain essentially amorphous up to $R = 20$. The crystalline-volume fraction is only 2–3% in the interface layers for high-H-diluted films with $5 < R < 20$. The detection of the c-Si Raman-active mode may be limited by both the small number and small size ($< 3\text{ nm}$) of the crystalline-grain seeds in the interface layers [29]. Interestingly, the bandwidth of the Raman spectra is about 120 cm^{-1} , which is much broader than the 70 cm^{-1} width in the surface layer as shown in Fig. 11a. The bandwidth exhibits no change with hydrogen dilution. This implies that the formation of the initial layer is affected by the glass substrate rather

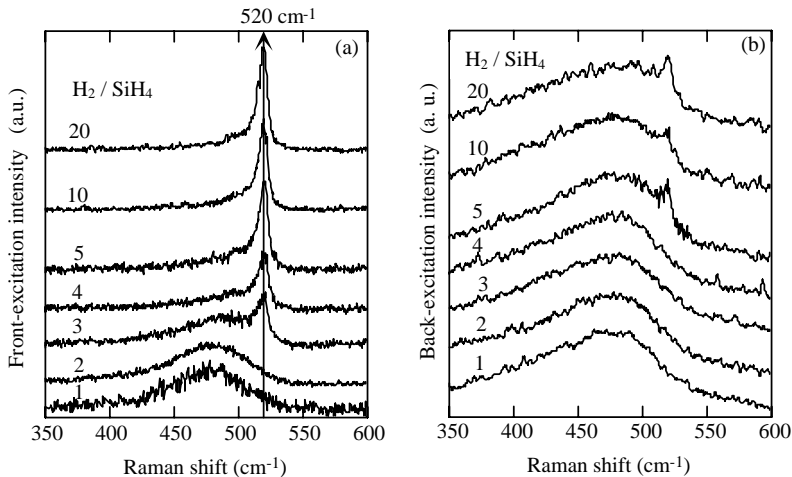


Fig. 11. Raman spectra from (a) front-excitation and (b) back excitation with 514.5 nm laser beam for group III films with various H-dilution ratios at $T_s=240^\circ\text{C}$.

than by H-dilution. Comparing the Raman spectra from the surface and the interface layer, one can see the same tendencies in all the films such as the narrowness of the 480 cm^{-1} band, the weakness of the 330 cm^{-1} LA and 445 cm^{-1} LO modes, and the enhancement of the 520 cm^{-1} c-Si mode. This indicates that the structural order is improved and the crystalline volume fraction is increased when the film grows thicker.

The PL spectra at 80 K from the top surface layer are shown in Fig. 12a. In addition to the broad a-Si PL band at $\sim 1.35\text{--}1.4\text{ eV}$, a much narrower band ($0.12\text{--}0.18\text{ eV}$) at $\sim 0.9\text{ eV}$ appears when $R > 3$, which is the H dilution ratio where the c-Si 520 cm^{-1} TO mode appears in Raman spectrum as shown in Fig. 11a. As the c-Si volume fraction increases with R , the a-Si:H luminescence fades away and the low-energy PL gradually dominates. Fig. 12b shows the PL spectra at 80 K from the interface layer. The PL from the a-Si phase dominates up to $R = 5$. The top two PL spectra show a dual-peaked feature correlated with the emergence of the c-Si peak in the Raman spectra. It is reasonable to find a correlation between Raman and PL spectra since both measurements probe the same layer of the materials by using the same wavelength 514.5 nm laser beam. We see that the PL energy position is quite sensitive to the changes of the microstructure. We have noticed the following interesting behavior of the low energy PL band: (a) the energy peak position shows a red-shift with an increase of H-dilution such as from 1.0 to 0.84 eV when R increased from 3 to 20 and the peak energy position is more greatly red-shifted in the surface than the interface layer. For the films with $R = 20$ and 10 , for example, the PL energy peaks at $0.84\text{--}0.87\text{ eV}$ and at $0.9\text{--}0.96\text{ eV}$ in the surface and the interface layer, respectively.

To compare the radiative centers in a thin layer with those in a thicker layer of the same film, we carried out the PL measurement with excitation by a 632.8 nm laser

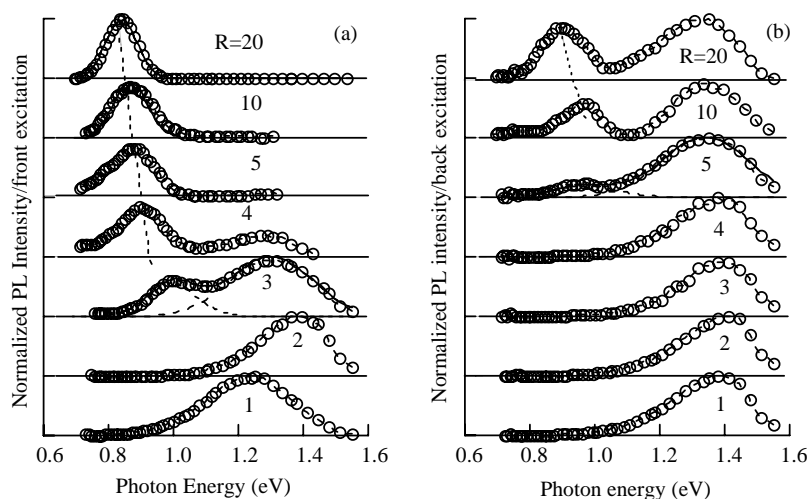


Fig. 12. PL spectra for (a) front- and (b) back excitation with 514.5 nm laser beam for the same films as in Fig. 11.

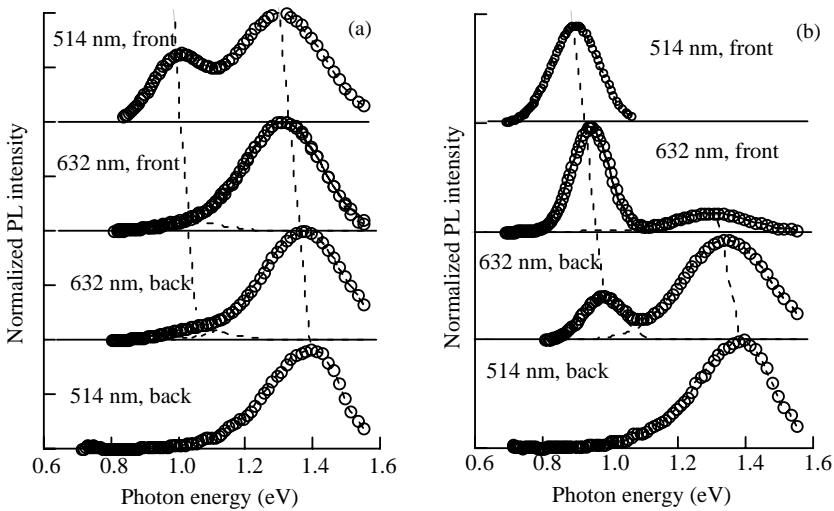


Fig. 13. PL spectra for films with (a) $R = 3$, and (b) $R = 4$ at $T_s = 240^\circ\text{C}$ using front- and back excitation with 514.5 and 632.8 nm laser lines.

beam where the penetration depth is ~ 0.3 to $\sim 1\ \mu\text{m}$ —roughly 5 times larger than for the 514.5 nm beam. Figs. 13a and b show the results for films with $R = 3$ and 4 using front- and back-excitation with 514.5 and 632.8 nm. In this way, the luminescence behavior has been sampled almost through the film from the interface to the surface layer. Let us examine the results, starting from the interface layer and moving through to the surface layer (i.e. from bottom curve to top curve in Figs. 13a and b). As the detected layer moves up closer to the surface, the common features of the PL spectra from these two films are (a) a more pronounced low-energy PL band, and (b) a red shift in the peak energy position for both the high-energy and the low-energy PL bands. These features result from an increase of crystalline volume fraction, as the film grows thicker.

3.5. Characteristics of the low-energy PL in $\mu\text{c-Si}$ films [2]

Based on the experimental results from both micro- and poly crystalline silicon films, there are two suggestions for the origin of the low-energy PL. In an early study, Bhat et al. [30] suggested that the 0.9 eV PL band results from recombination at defect centers in a much more ordered environment. More recently, Savchouk et al. [31] observed PL with a peak at $\sim 0.9\ \text{eV}$ in polycrystalline silicon films that contain c-Si grains and grain boundaries. They suggested that the 0.9 eV PL originates from tail-to-tail transitions in boundaries. The exponential tail states in polycrystalline silicon were calculated and examined by Werner et al. [32] using capacitance measurements. The structure of $\mu\text{c-Si:H}$ is somewhat different from poly-Si. It is a composition of crystalline grains embedded in a-Si:H matrix. The optical absorption spectra of $\mu\text{c-Si:H}$ films indicate that the electronic states in the

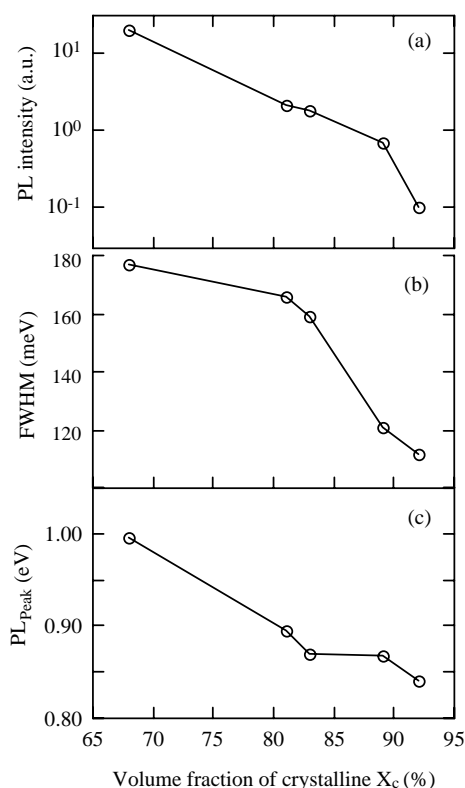


Fig. 14. The low-energy PL (a) total intensity, (b) FWHM, and (c) peak energy position, as a function of material crystallinity for the H-diluted films deposited at $T_s=240^\circ\text{C}$.

grain boundary (g.b.) region result in an absorption band that peaks at $\sim 1.25\text{ eV}$; the absorption spectral lineshape changes from a-Si:H-like to poly-Si-like when the film structure changes from a-Si:H to $\mu\text{c-Si}$ [3]. Taking into account the Stokes shift, the low-energy PL band more likely originates from the g.b. region.

We investigated the characteristics of the PL in the $\mu\text{c-Si:H}$ films listed in Table 2. Fig. 14 shows the low-energy PL intensity, the peak energy position, and FWHM as a function of X_c at 80 K. One can see that as the crystallinity increases: (a) the PL intensity decreases by about two orders of magnitude; (b) the band width decreases from 0.18 to 0.12 eV, and (c) the PL peak energy red shifts from 1.0 to 0.84 eV. We emphasize that the low-energy PL bandwidth is two times narrower in $\mu\text{c-Si}$ ($\sim 0.15\text{ eV}$) than the defect PL in a-Si:H (0.3 eV).

Fig. 15 shows the PL temperature and excitation intensity dependence. The spectra were taken of a film with $X_c=81\%$ using 632.8 nm excitation. One finds that the peak energy red shifts by about 170 meV from 15 to 180 K. According to the carrier thermalization model [1], the PL peak energy shift follows Eq. (1.5a). Using a reasonable value $\tau_r \approx 10^{-6}\text{ s}$, for the recombination lifetime of $\mu\text{c-Si}$ [33], one obtains $\text{PL}_{\text{peak}}(180\text{ K}) - \text{PL}_{\text{peak}}(15\text{ K}) \approx 180\text{ meV}$ that is very consistent with the experimental

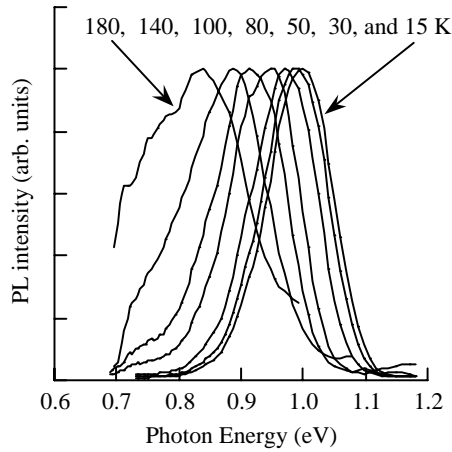


Fig. 15. Temperature dependence of PL spectra for the film $X_c=81\%$ using 632.8 nm excitation.

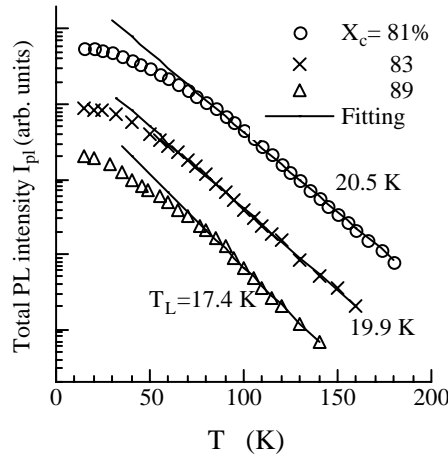


Fig. 16. I_{PL} vs. T for the films of $X_c=81\%$, 83% and 89% , respectively. The solid lines are fitted to the data based on Eq. (1.4).

observation. Fig. 16 plots the total PL intensity $I_{PL}(T)$ vs. temperature for samples with $X_c=81\%$, 83% , and 89% . One can see a weak temperature dependence of the PL intensity below 60 K which is similar to the characteristic of PL in a-Si:H. This has been explained as resulting from the non-radiative Auger processes at low temperatures [1]. Above 60 K, the PL intensity is rapidly quenched with the increasing temperature. Using Eq. (1.4) we obtain T_L equal to 21, 20 and 17 K, and the characteristic temperature of the exponential tail states, T_0 is equal to 283, 275, and 240 K for the samples with $X_c=81$, 86 and 89%, respectively. The value of T_0 is about two times smaller than $T_0=500$ K in a-Si:H. It is clear that T_0 decreases with

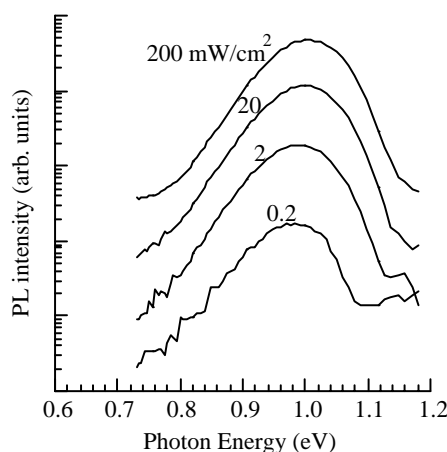


Fig. 17. Excitation intensity dependence of PL spectra at 15 K for the film $X_c = 81\%$ using 632.8 nm excitation.

increasing crystallinity. This is consistent with the observation of the decrease in PL bandwidth with increasing crystallinity as shown in Fig. 14b.

Fig. 17 shows the PL energy spectra at 15 K as a function of excitation intensity for sample T529. One can see that the PL peak shifts to high energy as the excitation intensity increases. This is simply due to the shift of the quasi-Fermi level position toward the band edge with increasing excitation intensity. The total intensity, I_{PL} , as a function of the excitation intensity, I_{ex} , for samples T529, T528 and T518 is shown in Fig. 18. One observes that the excitation intensity dependence shows two regimes. For high excitation intensity ($\geq 6 \text{ mW/cm}^2$), we found a sublinear relationship of $I_{PL} \propto I_{ex}^\gamma$ with an exponent of $\gamma \approx 0.65$ and an approximately linear dependence for low excitation intensity ($< 6 \text{ mW/cm}^2$). In general, at low temperature and low excitation intensity the carriers geminately recombine. Recombination becomes non-geminate when the electron–hole pair density exceeds about $2 \times 10^{18} \text{ cm}^{-3}$ [1].

4. Effects of hydrogen dilution, thickness and interface layer on a-Si:H i-layer and its solar cells prepared by PE-CVD

Plasma-enhanced CVD are commonly used in the a-Si:H solar cells industry. The most stable, high-performance a-Si:H solar cells were obtained by using hydrogen dilution of the reaction gas for the intrinsic layer [8,9,34]. An improved microstructure of the i-layer is responsible for the enhanced stability. TEM results suggested [34] that a-Si:H made with H dilution is a heterogeneous mixture of amorphous matrix and more ordered linear-like objects. X-ray diffraction (XRD) demonstrated [9,35] that the width of the first diffraction peak becomes narrower in the most stable material, indicating improved medium-range order. On the other hand, due to lack of sensitivity of Raman and XRD for obtaining crystalline silicon

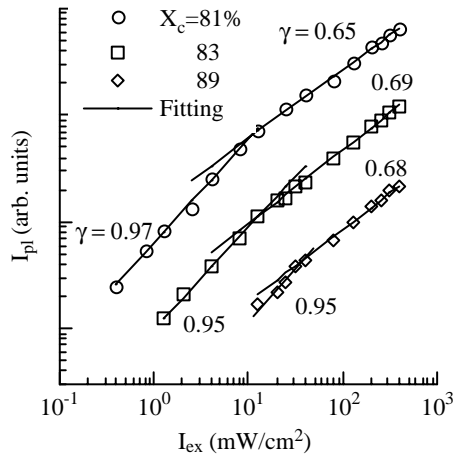


Fig. 18. Excitation intensity (I_{ex}) dependence of the PL integrated intensity (I_{PL}) for the film of $X_c = 81\%$, 83% and 89% . The open symbols are the experimental data.

signals for very small fractions ($\sim 1\%$) and/or small crystallite sizes, relevant electronic states have been studied by using transient photocapacitance spectroscopy [9] and the constant photocurrent method (CPM)[3]. The former showed an additional band at ≈ 1.2 eV and the latter showed an apparent shoulder at ≈ 1.25 eV in the optical absorption spectrum. Both were described as an indication of the presence of a small amount of microcrystalline Si (μ c-Si). Furthermore, the structure of these transition materials was found to be sensitive not only to hydrogen dilution but also to the substrate surface and the film thickness [9,35–37]. Here, we review the results on a series of films and their n-i-p solar cells made by PE-CVD using Raman and PL spectroscopy coupled with XRD and solar cell open-circuit voltage (V_{oc}) measurements.

4.1. Thickness and interface layer effects on a-Si:H film properties [36]

The films were deposited on stainless steel (ss) substrate covered with and without textured Ag/ZnO with the following three types of structures. Type I consists of ~ 0.5 μ m a-Si film deposited directly onto substrate, type II has the same structure as type I except that a thin amorphous n-layer was inserted between the substrate and the a-Si film, and type III is the same as type II except that the a-Si film has a larger thickness of ~ 1.5 μ m. These three structures were identical to those recently studied by Guha et al., using XRD and the capacitance profiling technique [9]. A thick sample #9883, deposited directly on ss substrates, was also measured. The sample parameters and microstructures are listed in Table 4.

Figs. 19a and b show Raman spectra for all the samples listed in Table 4. In Fig. 19a, all the spectra contain amorphous mode centered at ~ 480 cm^{-1} . Those are consistent with the XRD results. For sample #9883 in Fig. 19b, the narrow c-Si TO

Table 4
a-Si:H film characteristics with varied thickness and interface

Sample ID	Structure	Thickness (μm)	Features of $\mu\text{c-Si}$		
			XRD	Raman	PL
(a)	10306 ss/i	0.5	No	No	Yes
	10307 ss/n/i	0.5	No	No	No
	10311 ss/n/i	1.5	No	No	Yes
(b)	10857 ss/textured Ag/ZnO/i	0.5	—	No	Yes
	10859 ss/textured Ag/ZnO/n/i	0.5	—	No	No
	10858 ss/textured Ag/ZnO/n/i	1.5	—	No	Yes
(c)	9883 ss/i	1.4	Yes	Yes	Yes

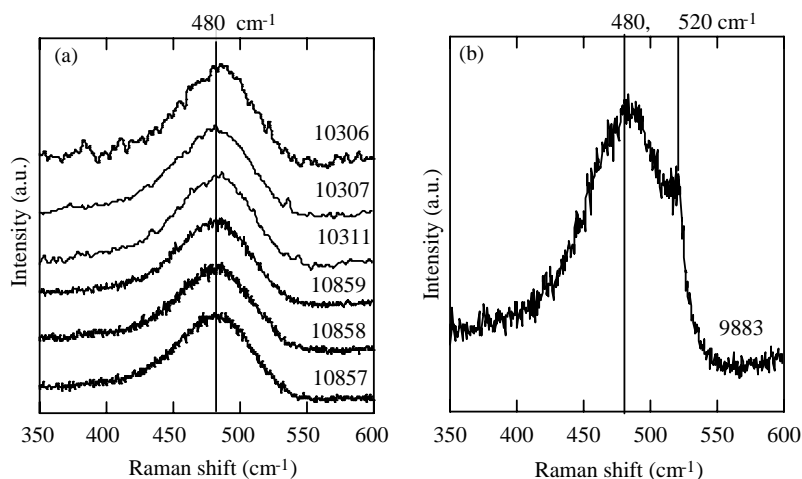


Fig. 19. Raman spectra for samples with thickness of 0.5–1.5 μm and different interface layers, (a) #10306, #10307, #10311, #10857, #10859, and #10858 showing a-Si TO mode only; and (b) #9883 with small c-Si mode.

mode at 520 cm^{-1} emerged, which is again in agreement with the results of XRD. We found that the FWHM of the broad 480 cm^{-1} Raman peak is the same for all the samples including #9883. Since the FWHM is proportional to the width of the bond-angle distribution, it is a measure for the short-range order of the film. Hence, the short-range orders of the a-Si:H network are all the same in the top surface layer except that a small volume fraction c-Si exists in sample #9883.

The PL spectra were measured using the same 514.5 nm laser excitation as was used for Raman. We have avoided the interference fringes. So, we compared the lineshape to figure out whether there is low-energy shoulder or not. The results are listed in Table 4. For the 0.5 μm thin films #10306 and #10857 deposited directly on

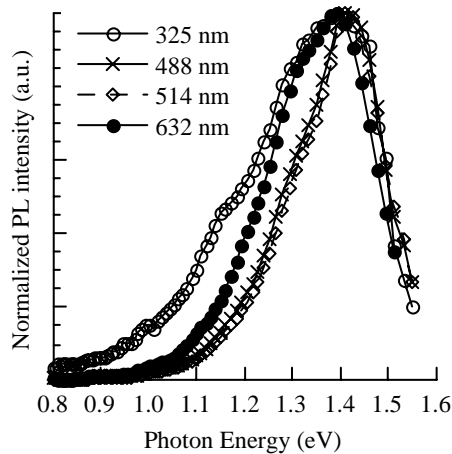


Fig. 20. Normalized PL spectra using 325, 488, 514, and 632 nm excitation for sample #9883 at 80 K.

the substrates without an n-layer, and for the 1.5 μm thick films #10311 and #10858 deposited on the substrates with a thin n-layer, the PL spectra at 80 K contains a low-energy shoulder at ~ 1.0 eV which indicates the presence of $\mu\text{c-Si}$ structures. Whereas, the sample with 0.5 μm thickness for either i/ss or i/n/ss substrate configurations there is only amorphous PL main band. Why did not we see any microcrystallinity by Raman spectra for the samples with a low-energy PL shoulder? The answer is either that the volume fraction of c-Si grain is below the Raman detection limit or that the c-Si size less than 3 nm [29]. Furthermore, the structural thickness dependence was measured by various PL excitation wavelengths. The 325 nm (3.81 eV), 488 nm (2.54 eV), 514.5 nm (2.41 eV) and 632.8 nm (1.96 eV) laser excitations correspond to penetration depths of 10 nm, 60 nm, 80 nm, and 1 μm , respectively. All the excitation-photon energies are greater than the band gap, i.e. intrinsic excitation, so the PL lineshape is not affected by the excitation wavelength but reflects the energy distribution of the recombination centers. The results are shown in Fig. 20 for the ~ 1.5 μm thick sample #9883. One can see that (a) an enhanced low-energy PL excited by 325 nm laser indicates $\mu\text{c-Si}$ structure in the top surface layer of 10 nm; (b) the PL spectra are dominated by the a-Si:H phase underneath the 60–80 nm layer; and (c) when the excitation laser passes through the whole film, the PL peak energy red shift indicates that the structural ordering is relatively poor in the initial growth layer. The changes of the PL lineshape imply non-uniform electronic states in the film growth direction, the same as described in Section 3.3 for HW-CVD films.

4.2. Electronic states of intrinsic layers in n-i-p solar cells near amorphous to microcrystalline silicon transition studied by PL [38]

The n-i-p solar cells were fabricated by PE-CVD on ss substrates covered by a textured back reflector. The reaction gas of disilane was diluted by hydrogen. Three

Table 5

V_{oc} and XRD data for solar cells their i-layers prepared with different H-dilution ratios (R) and thicknesses (d)

Cell no.	R	d (nm)	FWHM ($^{\circ}$)	μc fraction (%)	V_{oc} (V)
583	1.0	130	6.4(± 0.6)	0	0.962
591	1.0	220	5.3(± 0.3)	0	0.963
569	1.0	450	5.43(± 0.15)	0	0.984
592	1.2	105	5.1	0	0.955
600	1.2	215	5.8	0	0.973
576	1.2	410	4.98	4	0.766
593	1.6	110	4.5	~ 5	0.709
579	1.6	220	4.1	27	0.529
580	1.6	450	3.20	36	0.466

dilution ratios, $R = 1.0$, 1.2 and 1.6 were used, where $R = 1.0$ is the standard hydrogen dilution ratio, and $R = 1.2$ and 1.6 represent 20% and 60% more hydrogen dilution, respectively. The i-layer thicknesses were $d \approx 110$, 220, and 450 nm. The XRD measurements were done at the Colorado School of Mines [35]. The relevant cell deposition parameters, XRD results and V_{oc} are listed in Table 5. Among the nine samples studied, four of them show c-Si peaks in the XRD data. The microcrystalline volume fraction is estimated as the ratio of the sum of the (1 1 1), (2 2 0), and (3 1 1) peak areas to the total (a + μc) peak area [35]. It is clear that the μc -Si volume fraction increases as the hydrogen dilution and i-layer thickness increases. Meanwhile, the FWHM of the first a-Si:H peak tends to decrease with increasing H dilution and with increasing thickness for $R = 1.0$ and 1.6. This effect has been associated with improved medium-range order in the a-Si:H [35]. There is a clear correlation between the microcrystallinity and V_{oc} . In Table 5, high V_{oc} 's (> 0.95 V) were found for all cells that were detected to be fully amorphous, but low V_{oc} 's (< 0.9 eV) were found for all cells with the μc -Si component. In the cells with $R = 1.6$, one can see that the V_{oc} monotonically decreases from 0.709 to 0.466 V when the μc -Si volume fraction increases from $\sim 5\%$ to 36%. However, XRD and Raman may lack the sensitivity to distinguish the changes in the material properties in the cells below the onset of microcrystallinity such as the five cells with $R = 1$ and 1.2, particularly for the thinner i-layers which lead to the rather large experimental uncertainties in FWHM listed in Table 5. A more sensitive technique is desirable.

The ~ 1.0 eV PL band was found to be a characteristic feature of μc -Si from a series of HW-CVD transition films [2]. Since the properties of the electronic states are crucial for solar cell performance, we study these transition materials by using PL spectroscopy. We show the normalized PL spectra at 80 K for the cells below and above the transition, from fully amorphous to partially microcrystalline in Figs. 21a and b, respectively. In Fig. 21a the PL lineshape shows the effects of both hydrogen dilution and thickness, although the samples did not show any detectable c-Si signal by XRD. When d is increased from 110 to 220 and 450 nm in the solar cells with $R = 1.0$ at the bottom of Fig. 21a, the PL peak energy is blue shifted from 1.36 to 1.39 and 1.42 eV. At the same time, there is an enhancement of the low-energy

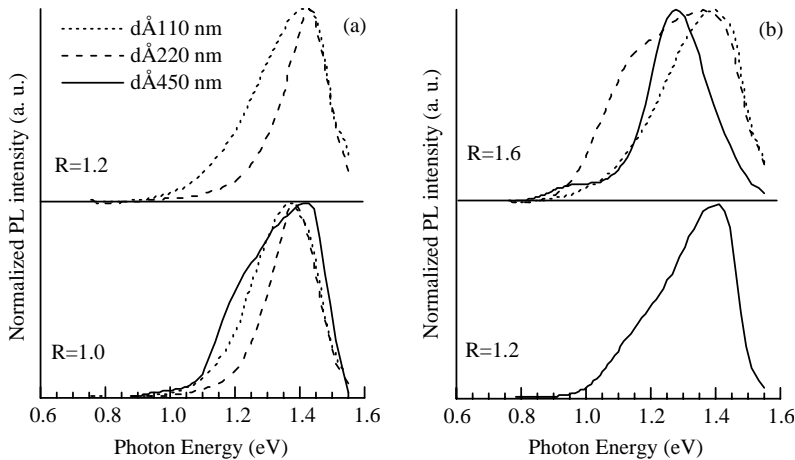


Fig. 21. Normalized PL spectra at 80 K for (a) five cells of #583, #591, #569, #592 and #600 that are below XRD-detectable microcrystallinity, and (b) four cells of #576, #593, #579 and #580 that are above the XRD-detectable transition to mixed a-Si:H/ μ c-Si. The dotted, dashed, and solid lines correspond to $d \approx 110$, 220, and 450 nm, respectively.

shoulder (~ 1.2 eV). The thickness effect is more clearly shown for the two cells with $R = 1.2$, i.e. the two spectra at the top of Fig. 21a, in that the FWHM of the PL main-band decreases from 0.3 to 0.2 eV as the i-layer is increased from 110 to 220 nm. On the other hand, in Fig. 21b we see that for the cells with μ c-Si volume fractions from 4% to 36% characterized by XRD, the PL main features are (a) the total PL intensity decreases by a factor of 4–5 compared to a-Si:H cells because of the decrease of the radiative recombination from the a-Si:H matrix; and (b) there is no longer a blue shift of the PL peak energy because of the relatively large intensity of the 1.2 eV band. The top curves of Fig. 21b show that the 1.2 eV PL band dominates in the cells with μ c-Si volume fraction of 27–36%.

We explain the above observations as follows. First, the increased hydrogen dilution results in an improvement of the medium-range order of the amorphous network. We believe that this results in a narrowing of the valence band tail [2,8] and then a PL blue shift along with a decrease of the bandwidth. The network order is also improved when the i-layer grows thicker. Second, we believe that a small percentage of crystalline silicon grains, perhaps with small sizes, have gradually emerged in the a-Si:H matrix when increasing either hydrogen dilution or the film thickness. This is indicated by the enhancement of the 1.2 eV PL shoulder in the a-Si:H cells as shown in Figs. 21a and b. When the crystalline grains become measurable by XRD, the PL peak energy is red shifted because of the enhancement and finally dominated by the 1.2 eV PL band in the μ c-Si cells.

To explore the nature of the 1.2 eV low-energy PL bands, we study the temperature dependence of the PL spectra. In Fig. 22 we plot a typical group of PL spectra at 200 K from cells of $d \sim 220$ nm with $R = 1.0$, 1.2 and 1.6. All the three PL spectral lineshapes are completely different from that of typical a-Si:H samples at

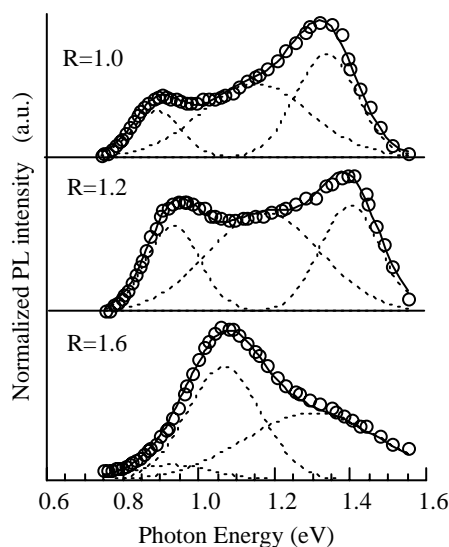


Fig. 22. Normalized PL spectra at 200 K for cells #591, #600, and #579 with $d \approx 220$ nm and $R = 1.0, 1.2$ and 1.6 . Open circles represent experimental data. Dotted lines are Gaussian functions with their superpositions indicated by the solid lines.

200 K. A notable feature is that the relatively large intensity of the 1.2 eV PL band finally becomes dominant in the $R = 1.6$ cell. The other interesting feature is that the 0.9 eV band is also relatively large in the $R = 1.0$ and 1.2 cells. We believe that both features originate from the enhanced radiative recombination in the c-Si grain boundary regions. These spectra consist of three components and can be fitted with Gaussian functions peaked at ~ 0.9 , ~ 1.06 – 1.2 , and ~ 1.33 – 1.4 eV. In Section 3, we have suggested that an electronic sub-band is formed from the grain boundary region of $\mu\text{c-Si}$ films prepared by HW-CVD and the 1.0 eV PL originates from the tail-to-tail transition in that region according to the carrier thermalization model following Eq. (1.2) $I_{\text{PL}} = I_0 \exp(-T/T_0)$. Here, we plot a group of typical I_{PL} vs. T curves in Fig. 23. The solid lines are least-square fits yielding $T_0 = 21$ and 34 K from the I_{PL} for 1.4 and 1.2 eV PL bands, respectively. The former is compatible with the observed value of 23 K in a-Si:H films [1], the latter is attributed to the tail-to-tail transitions in the grain boundary regions. Whereas, the energy position is higher and the temperature dependence is weaker than the low-energy PL band in $\mu\text{c-Si:H}$ prepared by HW-CVD. The dashed line and diamond symbols in Fig. 23 represent the data from the 0.9 eV defect band of cell #600. The weak temperature dependence is similar to that in typical a-Si:H films [1]. It is worthwhile to mention here that the relatively strong 0.9 eV PL band in the films just before the onset of micro-crystallinity does not mean a high defect density. It indicates more radiative transitions via dangling bond states in these films than that in non-hydrogen diluted a-Si:H films.

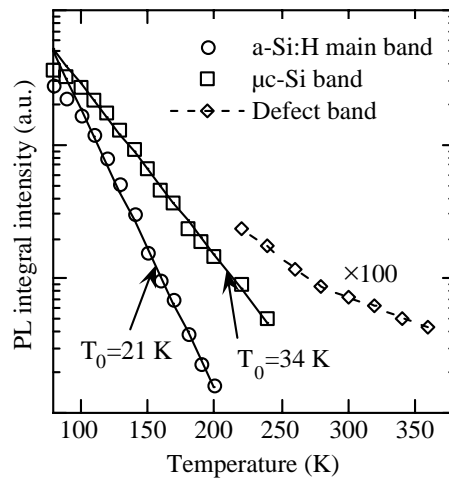


Fig. 23. Integrated PL intensity (I_{PL}) vs. temperature. Open circles and squares correspond to the experimental data of ~ 1.4 , ~ 1.2 eV bands from cell #579, and diamonds correspond to the data of 0.9 eV PL bands from cell #600. Solid lines are the fits based on $I_{PL} = I_0 \exp[-T/T_0]$.

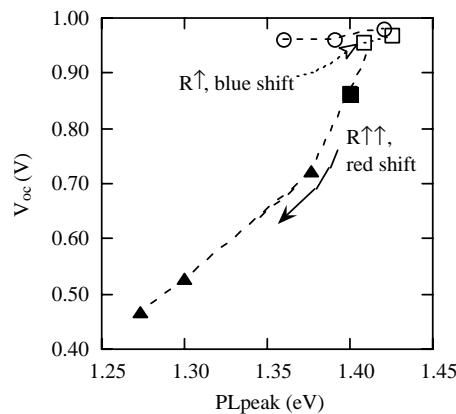


Fig. 24. V_{oc} as a function of the PL peak energy position for the nine near-transition solar cells studied. The open circles and squares represent the five cells shown in Fig. 21(a). In this regime, V_{oc} increases as the PL is blue shifted. The solid symbols represent the four cells shown in Fig. 21(b). In this regime, the V_{oc} rapidly decreases as the PL is red shifted due to microcrystallinity.

Distinguished by the onset of microcrystallinity characterized by XRD, we found that there are two regimes of the PL features for the nine solar cells near transition as shown in Fig. 24. In the five cells below the onset of detectable microcrystallinity, the dominant factor of increase hydrogen dilution and thickness is to improve the a-Si:H structural order. As a result, the PL peak energy is blue shifted and the linewidth is narrowed. In the four cells above the onset of microcrystallinity, the main factor is an increase of the μ c-Si volume fraction, which results in the decrease of the total PL intensity and the increase of the 1.2 eV PL band. Meanwhile, the V_{oc} quickly

decreases as the PL energy is red shifted. Proper conditions such as a combination of hydrogen dilution ratio and thickness at $R = 1.0$, $d = 0.2\text{--}0.4\text{ }\mu\text{m}$ and $R = 1.2$, $d = 0.2\text{ }\mu\text{m}$ have produced the highest V_{oc} as shown in Fig. 24 and Table 5. These are consistent with the most stable high-performance a-Si:H solar cells prepared just before the onset of microcrystallinity [9,34].

5. Luminescence in a-Si:H p-i-n diodes under double injection (dispersive-transport-controlled recombination) [39,40]

In this section we review the EL results in a-Si:H p-i-n and n-i-p diodes. Comparing the thermalization-controlled geminate recombination processes of PL to the features of EL, the differences can be explained by transport-controlled non-geminate recombination in trap-rich materials. EL arises from recombination of non-geminate e-h pairs because the electron and hole are injected from opposite sides of the diode. Regardless of the generation methods, one would expect similar recombination processes in both EL and PL. However, significant differences in the features of EL and PL in the same p-i-n or n-i-p structures have been observed such as the low efficiency and the low peak energy of EL. In earlier EL studies [41–43], the low EL efficiency was explained by the fact that the recombination only takes place near the p-i interface, and the low peak energy was explained by optical interference effect. We have presented the following new model to explain the features of EL based on systematic experimental studies.

5.1. The model of EL in a-Si:H diodes under double injection

5.1.1. EL generation rate

It is common to calculate an effective generation rate g for an EL from the forward bias current density [41–43]. Then, $g = J_F/eL$ where J_F is the forward-bias current density, e is the charge of an electron, and L is the i-layer thickness. This is valid if every carrier across the junction recombines within the device. The forward bias current equals the recombination current, $J_F = J_r$; in other words, the carrier recombination lifetime τ is less than or equal to the transit time t_0 . When the condition $\tau \leq t_0$ is not met, in other words, when the injection current is larger than the recombination current, gain $(\tau/t_0) > 1$, the forward bias current is approximately [44]

$$J_F = J_r(\tau/t_0) \quad [\text{A cm}^{-2}]. \quad (5.1)$$

This implies that before one injected, electron recombines with a hole in the device it circulates in the circuit τ/t_0 times. We found the factor (τ/t_0) to be as large as $10^2\text{--}10^3$ in photogain measurements [45]. So, the generation rate for EL can be expressed as

$$g = (J_r/eL) = (J_F/eL) \times (t_0/\tau) \quad (5.2)$$

or

$$g = J_F / eL \quad \text{when } (\tau / t_0) \leq 1. \quad (5.3)$$

Then the EL efficiency is

$$\eta = \frac{I_{EL}}{J_F / eL} \left(\frac{\tau}{t_0} \right)$$

that is as high as the PL efficiency. In the following, the EL peak energy position is described by the model of dispersive-transport-controlled recombination.

5.1.2. The critical energies of carrier transport and recombination in trap-rich materials

In amorphous semiconductors, the localized states having exponentially decaying distributions toward the gap center affect the recombination processes as well as the transport. It is commonly accepted that the carrier transport in disordered materials is trap-limited and it can be described by the so-called multiple trapping (MT) model [6,7], in which the carriers are frequently trapped in tail states and released by thermal excitation. In the MT model the carrier transport is considered to be taking place at the mobility band edge and, at certain times, the average trap energy of the carriers is given by the demarcation level E_D ,

$$E_D = kT \ln(v_0 t) \quad \text{when } T < T_0. \quad (5.4)$$

E_D is defined as the energy at which the thermalization rate v_0 is equal to the reciprocal of the observation time t in carrier transport measurement. E_D is defined the same as that in Eq. (1.4) in which the carrier's lifetime τ_r is used instead of t . The deepest energy position of the demarcation energy E_D is the bottom of the tail states, that is about 0.3–0.35 eV above E_v and 0.1–0.15 eV below E_c for the holes and electrons, respectively. The phonon-assisted transition rate (thermalization rate) $v_0 \approx 10^{12} \text{ s}^{-1}$ is greater than both the radiative- and non-radiative recombination rate, 10^3 – 10^4 and 10^6 – 10^7 s^{-1} . Therefore, the luminescence occurs only after the majority of carriers have thermalized to sufficiently low density of states. Further phonon-assisted transitions are suppressed by the weak overlap to neighboring sites. In addition to the Stokes shift, the tail-to-tail luminescence peak energy reflects the carrier distribution in the tail states and is expected to have a time- and temperature shift as shown in Eq. (1.5). The thermalization model [1] also describes the temperature dependence of PL efficiency as shown in Eq. (1.4).

In the case of EL, we found that both the energy peak position EL_{peak} and its temperature dependence do not follow the thermalization model, especially at low temperatures. We suggest that the carrier transport has to be considered as a determining factor. The MT model provides a good description of the transport phenomena for temperature greater than 200 K. At lower temperatures, hopping transport in the exponential band tail (or through potential fluctuations) must be considered. The carrier transport then is no longer near the band edge E_c (E_v) but at the transport level E_t that has been introduced by Monroe [5]

$$E_t = kT_0 \ln(8/27R_0^3 N_0) - 3kT_0 \ln(T_0/T). \quad (5.5)$$

The first term is an energy that is estimated to be close to the mobility edge, so that the second term represents the shift of the transport path below E_c (above E_v for holes). Both hopping-up and hopping-down processes are permitted within band tails at about $T > 200$ K; below this temperature, only hopping transition to states of lower energy occurs [5]. At about $T > 200$ K the second term in Eq. (5.5) becomes very small, thus $E_t \approx E_c$ ($\approx E_v$ for holes) and the MT model is valid. When the band-tail distribution is broad (a greater T_0) and at low temperatures such that $T < T_0$ the electron transport level shift below E_c (above E_v for holes) is most significant. Furthermore, in the dispersive regime ($T < 200$ K for electrons, $T < 350$ K for holes), it has been found that the carrier drift mobility increases as the field increases, in the same manner as it increases with increasing temperature. In other words, the carriers transport level shifts towards the band edge with increasing electric field in that temperature range.

We first discuss the role of the critical energies $E_D(T)$ and $E_t(T)$ in the forward bias current. The steady-state forward current in a-Si:H p-i-n and n-i-p diode is a recombination limited current [46]. We discuss the applied-field range of $2\text{--}10 \times 10^4$ V/cm in which both the recombination-rate and the current spatial distribution are uniform through the i-layer according to a numerical calculation. Hence, one can obtain the properties of the i-layer from the measurements. The forward current is dominated by the electrons because they move much faster than the holes. Thus, the forward current density is $J_F \cong J_n = \mu_n \tau_n E$. Fig. 25 shows the

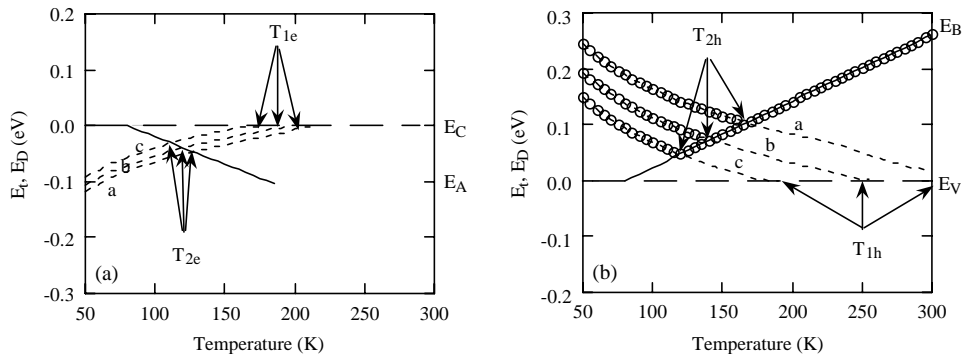


Fig. 25. (a) Calculated $E_t(T)$ and $E_D(T)$ positions as a function of temperature for electrons. E_c and E_A indicate the conduction-band edge and the bottom of the conduction-band tail, respectively. The solid line corresponds to $E_D = -kT \ln(v_{0tr})$, and the dashed lines correspond to $E_t = -3kT_0 \ln(T_0/T)$, by using $v_{0tr} = 10^5$, $T_0 = 300$ K. The dashed lines a, b, and c correspond to the electric field $2, 4$, and 6×10^4 V/cm, respectively. (b) Calculated $E_t(T)$ and $E_D(T)$ positions for holes as a function of temperature. E_v and E_B indicate the valence-band edge and the bottom of the valence-band tail, respectively. The solid line corresponds to $E_D = kT \ln(v_{0tr})$, and the dashed lines correspond to $E_t = 3kT_0 \ln(T_0/T)$ by using $n_{0tr} = 10^6$, $T_0 = 450$ K. The open circles indicate the tunneling transition energy for EL_{peak} . The crossing point of $E_t(T)$ and $E_D(T)$ indicate the temperature, T_{2h} , where the carrier's transport mechanism changes. T_{1h} indicates the temperature where the demarcation level has reached the bottom of the tail. The dashed lines a, b, and c correspond to the electric field $2, 4$, and 6×10^4 V/cm.

calculated $E_D(T)$ and $E_t(T)$ positions as a function of temperature for electrons according to Eqs. (5.4) and (5.5) by using $v_0\tau_r=10^5$ (with a non-radiative recombination lifetime $\tau_r=10^{-7}$ s) and $T_0=300$ K. The transport level $E_t(T)$ represents the balance of hopping and thermal excitation to $E_t(T)$; it shifts to the band edge with an increase in temperature. The demarcation level $E_D(T)$, on the other hand, represents the balance of thermal excitation to the band edge and re-trapping into the tail states; it shifts away from the band edge with an increase in temperature. Considering the increase of the electric field in the same manner as an increase of temperature, we calculated the transport levels, $E_t(T)$, at an electric field equal to 2, 4, and 6×10^4 V/cm. For a better fit to the experimental results of both the current and the luminescence, we consider the thermalization by multiple trapping above 80 K in the calculation. There are two transition temperatures, T_{2e} and T_{1e} , in the figure. When $T < T_{2e}$, the transport energy level E_t is deeper than the thermalization energy E_D , and electrons move along at E_t . The cross points of $E_t(T)$ and $E_D(T)$, $T_{2e} \approx 110, 120$, and 125 K, indicate the temperature where the carrier transport mechanism changes from hopping-controlled to MT regime where the electrons move still along E_t . The other transition temperature $T_{1e} \approx 180, 190$, and 200 K, indicates the temperature where the transport energy level has reached the conduction-band edge E_c . Meanwhile, at a temperature of about T_{1e} the electron demarcation level E_D has reached the bottom of the conduction tail E_A . When $T > T_{1e}$, the carriers move along the conduction-band edge; then the carrier transport can be described by a ballistic model (free carriers drifting to a center) in steady-state measurements while dispersive behaviors still can be seen in transient processes. We now discuss the role of the critical energies $E_D(T)$ and $E_t(T)$ in the EL. Because the valence band tail is much broader than the conduction band tail, the features of the EL are dominated by valence band tail states. According to Eqs. (5.4) and (5.5), we use $v_0\tau_r=10^8$ (with a radiative recombination lifetime $\tau_r=10^{-4}$ s) and $T_0=450$ K for holes. Fig. 25 shows the calculated demarcation energy and transport energy positions as a function of temperature and electric field for holes. At temperatures $T < T_{2h}$, the hopping controlled regime determines the carriers transport and the transport level E_t is deeper than E_D in the tail. The EL_{peak} is lower than the PL_{peak} because the transport level $E_t(T)$, rather than $E_D(T)$, controls the EL processes. $E_t(T)$ crosses $E_D(T)$ at temperature, $T_{2h} \approx 115, 135$, and 155 K, where T_{2h} decreases with increasing electric field. The demarcation energy is deeper than the transport level in this regime, so the radiative tunneling occurs from E_D with high probability and the EL energy peak position will be controlled by the demarcation energy. At $T_{1h} \approx 190, 250$, and 310 K, the transport level reaches the valence band edge E_v causing the free carriers to be captured by deep states more efficiently. Thus, recombination via defects will dominate. Meanwhile, at a temperature about T_{1h} the hole demarcation level E_D has reached the bottom of the valence tail E_B . This implies that the tail states are in thermal equilibrium with the band edge, thus the probability of the tail-to-tail radiative transition is very low. Consequently, one observes dominating defect EL for $T > T_{1h}$.

The features of both the forward current and the EL temperature and electric field dependence as well as the EL energy spectrum in p-i-n structures can be explained

by using the temperature dependence of the characteristic energy curves in Fig 25a and b.

5.2. Sample and experimental conditions

Device quality a-Si:H p-i-n diodes were made on transparent-conducting-oxide (TCO) coated-glass and n-i-p on TCO coated ss substrates by PE-CVD, and p-i-n diodes by photo-enhanced CVD techniques. The TCO was textured to avoid interference fringes, except for one pair of 1.0 μm thick identical samples deposited on both textured and smooth surfaces that were used to insure that the structure of the EL spectrum is not due to optical interference effect. The top contacts were Ag, Al or ZnO, the area was 0.1–0.3 cm^2 . The i-layer thicknesses L were 0.2, 0.3, 0.4, 0.5, 0.53, 0.55, 1.0, 1.1, 2.0 and 10.0 μm . Samples with $L \leq 0.55 \mu\text{m}$ are called thin samples while $L \geq 1 \mu\text{m}$ are called thick samples. Among them, the high performance a-Si:H p-i-n solar cells were made by d.c. glow discharge at BPSolar. The 0.5 μm intrinsic layers were made of either hydrogen-diluted silane or pure silane, denoted as p-i_H-n and p-i-n, respectively [8].

States A and B denote the initial and the photo-degraded state of the p-i-n diode, respectively. The photo-degraded state was reached by exposing the sample to a 200 mW/cm^2 white light with an infrared-cut-off filter. From 8 to 1000 h light-soaking through the glass side of the sample was used to reach State B.

For EL measurements, the applied voltage was obtained from a programmable pulse generator. A 10 Hz repetition rate with 10 ms pulse width was typically used. We varied the forward bias current density between 10^{-4} and $10^2 \text{ mA}/\text{cm}^2$. The contribution of thermal radiation to the signal was less than 2% of the total signal [47]. The temperature dependence of the EL efficiency was measured under constant voltage condition. The sample temperature range was 30–350 K.

5.3. Results

5.3.1. Temperature dependence of the forward bias current

We show the temperature dependence of the forward current density J_F from the thin and thick a-Si:H p-i-n and n-i-p samples in their initial states A. Figs. 26a and b show the J_F vs. $1/T$ curves for a pair of 0.5 μm cell with and without hydrogen dilution, p-i_H-n and p-i-n, under 2, 3, and 4 V bias. The electric field across the i-layer is $V_i/L = (V_a - V_{bi})/L$, where V_a is the applied voltage and $V_{bi} = 0.8 \text{ V}$ is the built-in potential. The general picture of the current temperature dependence shows three regions corresponding to the three regions in Fig. 25a:

- (a) $T < T_{2e}$, the low temperature hopping transport regime: the injected carriers move along the transport level E_t that is deep down to the tail states as shown in Fig. 25a. The weak temperature dependence of the current is due to a small activation energy of $\mu_n \tau_n$, that is about 0.01 eV, reasonably for the hopping activation energy.

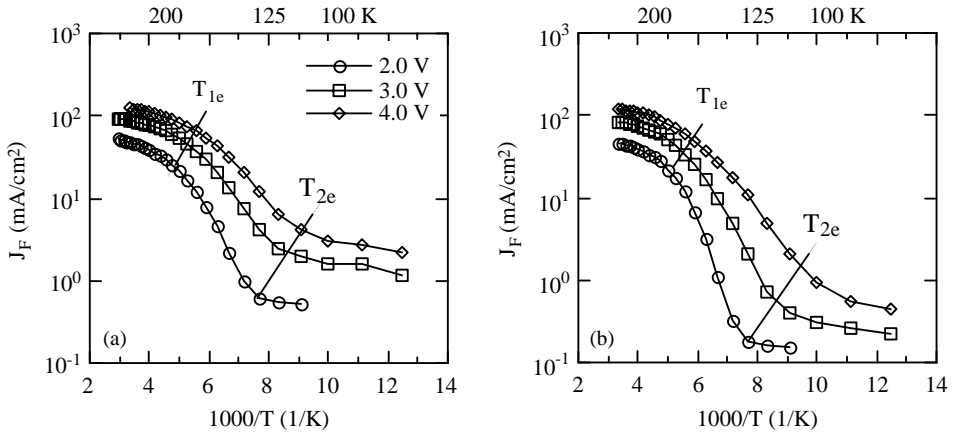


Fig. 26. Forward current density J_F as a function of temperature from (a) $0.5 \mu\text{m}$ p- i_H -n diode, (b) $0.5 \mu\text{m}$ p-i-n diode under 2.0, 3.0, and 4.0 V bias. Two transition temperatures T_{1e} and T_{2e} are indicated.

- (b) $T_{2e} < T < T_{1e}$, the multiple-trapping (MT) regime: the transport level E_t is above the demarcation level E_D . The carriers are still moving along at E_t where it is very close to E_c . The current is thermally activated with an activation energy of $\mu_n \tau_n$. In Fig. 26a, one obtains the transition temperature T_{2e} at 110–120 K that is consistent with the calculated curves in Fig. 25a. For electric fields 2, 4, and 6×10^4 V/cm in the $0.5 \mu\text{m}$ p- i_H -n diode, the activation energies are 0.08, 0.095, and 0.13 eV that agree well with the results from electron drift mobility measurements [48]. The variation of the activation energy is due to the field dependence of the drift mobility. In Fig. 26b an activation energy of 0.09, 0.13, and 0.2 eV for the p-i-n cell was found. The smaller activation energy in the p- i_H -n cell than that in the p-i-n cell indicates a narrower conduction band tail in the p- i_H -n cell.
- (c) $T > T_{1e}$, the transport level E_t has already reached the conduction-band edge E_c . The carrier transport is assumed to be of a ballistic type, thus the current is no longer thermally activated. However, the dispersive behavior still can be seen in transient measurements. The calculated T_{1e} is about 200 K in agreement with the experimental T_{1e} in Figs. 26a and b.

These three regions of forward current temperature dependence are not always observed simultaneously in one curve. For thin samples at a high-applied field, one may only observe a weak temperature dependence of the current. When the high field pushes T_{1e} down to lower temperature close to T_{2e} , one would not observe the thermal activated regime of $T_{2e} < T < T_{1e}$.

5.3.2. Temperature dependence of the EL efficiency

The carrier transport plays a role in the temperature dependence of EL. One should keep the generation rate constant in the measurement of temperature dependence of the luminescence efficiency. We have suggested using a constant

voltage instead of a constant current because of the gain factor, $(\tau/t_0) > 1$. The argument about the gain factor will be valid in the temperature range $T > T_{2c}$ where the MT model is valid, in other words when the carrier transport takes place near the mobility edges. The carrier's mobility will decrease rapidly in the hopping transport regime when $T < T_{2c}$, and the gain factor tends to be one.

The EL efficiency can be written as the total emission intensity per generation rate per unit area A ,

$$\eta_{EL} = I_{EL}/Ag = (I_{EL}/I_F) \times e\mu_n\tau_n(V_i/L). \quad (5.6)$$

The total emission from the sample is I_{EL} , and the forward current is $I_F = AJ_F$. Assuming that a small thermal activation energy of $\mu_n\tau_n$ product can be taken into account later, the factor $\mu_n\tau_n(V_i/L)$ does not change with temperature under constant voltage. Thus, I_{EL}/I_F is the effective EL efficiency in temperature dependence measurements under constant voltage condition. In other words, a constant voltage (not a constant current!) with a modification of the activation energy of $\mu_n\tau_n$ means a constant generation rate in the EL efficiency temperature dependence measurements.

We show the experimental results of EL effective efficiency, I_{EL}/I_F , as a function of temperature for the $0.5\mu\text{m}$ p-i-n and p-i-n cells in Figs. 27a and b. As the temperature increases there are three regimes in the I_{EL}/I_F vs. T curves:

- $T < T_{2h}$, the efficiency I_{EL}/I_F increases rapidly with temperature and depends on the applied voltage. The EL efficiency shows a maximum value at a transition temperature T_{2h} , and the maximum efficiency varies with applied voltage, higher fields corresponding to a lower T_{2h} and higher efficiency.
- $T > T_{2h}$, the efficiency I_{EL}/I_F decreases with temperature and does not depend on the applied voltage. It is reasonable that the I_{EL}/I_F vs. T curves do not depend on voltage for $T > T_{2h}$, if the luminescence efficiency depends on the generation rate linearly.

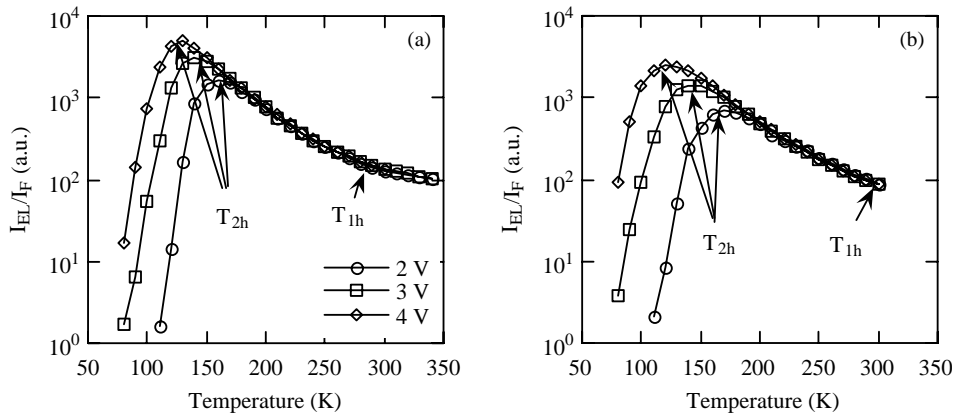


Fig. 27. EL effective efficiency I_{EL}/I_F as a function of temperature for (a) $0.5\mu\text{m}$ p-i-n and (b) $0.5\mu\text{m}$ p-i-n diodes at 2.0, 3.0, and 4.0 V bias, the transition temperatures, T_{2h} , are indicated.

- (c) When T is near room temperature, $I_{\text{EL}}/I_{\text{F}}$ does not change much with temperature due to the defect EL_{d} domination. It is shown more clearly in Fig. 27a at $T > 250$ K. The enhancement of defect luminescence in EL comparing to PL will be discussed later.

We explain the experimental results in Figs. 27a and b using the calculated curves in Fig. 25b for holes because the hole distribution in the valence band tail is the dominant factor for the luminescence signal. When $T > T_{2\text{h}}$, one expects the transport to be hopping-controlled. As the temperature decreases, $I_{\text{EL}}/I_{\text{F}}$ decreases because the deeper the transport level the less the wave functions overlap; consequently, the tunneling rate for EL decreases exponentially according to Eq. (1.2), $P_{\text{r}} = P_0 \exp(-2R/R_0)$. Meanwhile, the EL efficiency is enhanced by an increase in the applied field. This field-enhanced transition can only be seen in the case of non-geminate recombination. An opposite situation occurs in geminate recombination processes where the field quenches PL [49]. When $T > T_{2\text{h}}$, the EL effective efficiency $I_{\text{EL}}/I_{\text{F}}$ decreases with a temperature similar to the PL efficiency that follows the thermalization mode [1] We found the slope of the EL main band $T_{\text{L}} = 29$ K in the p-i-H-n and $T_{\text{L}} = 37$ K in the p-i-n cell [8]. This indicates a narrower valence band tail in the p-i-H-n than in the p-i-n cell according to Eq. (1.4). These results are consistent with those from J_{F} activation energy data shown in Figs. 26a and b.

It is clear that the transition temperature $T_{2\text{h}}$ depends on the applied field. In Fig. 28, we plot the $T_{2\text{h}}$ as a function of the electric field from a group of a-Si:H p-i-n diodes including the data in Figs. 27a and b. One can see that the data show a decrease of $T_{2\text{h}}$ proportional to the field in a good agreement with the field effect on the carrier dispersive-transport [48].

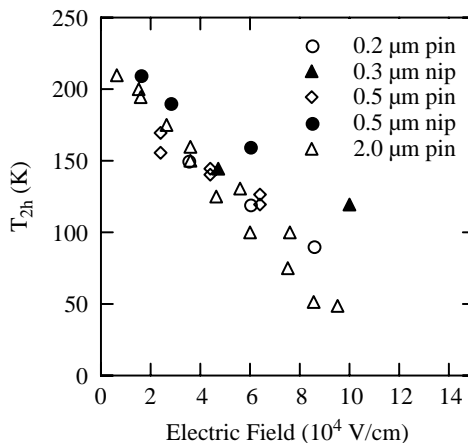


Fig. 28. $T_{2\text{h}}$ as a function of the electric field across the i-layer for 0.2, 0.3, 0.5, and 2.0 μm p-i-n and n-i-p samples.

5.3.3. Temperature and electric field dependence of the EL energy peak position

It has been a puzzle why the EL peak energy is always lower than the PL peak energy of the same sample [41–43]. We show the temperature dependence of EL spectra at the initial state A from both a thin and a thick p–i–n samples. In order to compare the spectral lineshapes, the spectra were normalized to the same integral EL intensity. Fig. 29a shows EL spectra from a 0.2 μm thick p–i–n diodes at 2.5 V applied voltage. Both the main- and the defect-band can be seen clearly at $T > 200$ K in thin samples. Fig. 29b shows EL spectra from a 2.0 μm thick p–i–n diodes at 20 V. The EL defect-band is very weak in thick p–i–n samples and similar to the weak PL defect signal. We notice that at low temperature in both thin and thick samples the EL main band peak energy EL_{peak} is about 1.2 eV. There is a thickness dependence of the EL spectral lineshape [47]. The main band is relatively strong in thick samples with $L \geq 1 \mu\text{m}$, but the defect band is relatively strong in thin samples with $L \leq 0.55 \mu\text{m}$.

To compare the main band peak energies between EL and PL, we plot in Fig. 30 the main band luminescence peak energy as a function of temperature for both PL_{peak} and EL_{peak} from 0.2, 0.4, and 2.0 μm p–i–n diodes. One can see that the $\text{PL}_{\text{peak}}(T)$ follows the thermalization model, while the $\text{EL}_{\text{peak}}(T)$ does not. The PL spectra were measured with 0.1 W/cm^2 514.5 nm laser excitation, and the EL spectra were measured under $2 \times 10^4 \text{ V/cm}$ applied field. One sees that the $\text{EL}_{\text{peak}}(T)$ temperature dependence is very weak in a wide temperature range of 50–300 K. The EL peak energy position can also be discussed according to the characteristic energies shown in Fig. 25b. Since the carrier's hopping rate is much faster than the recombination rate, the carriers first hop down to their transport energy level and circulate many times through the device then recombine from their transport levels. Therefore, when $T < T_{2h}$, the EL_{peak} is controlled by the transport level $E_t(T)$ which is about 0.2 eV deeper than the energy position of $E_D(T)$ at low temperatures. When $T > T_{2h}$ the energy position of $E_D(T)$ is lower than $E_t(T)$, the transition occurs then with higher probability between the $E_D(T)$. Thus, the EL_{peak} will follow the

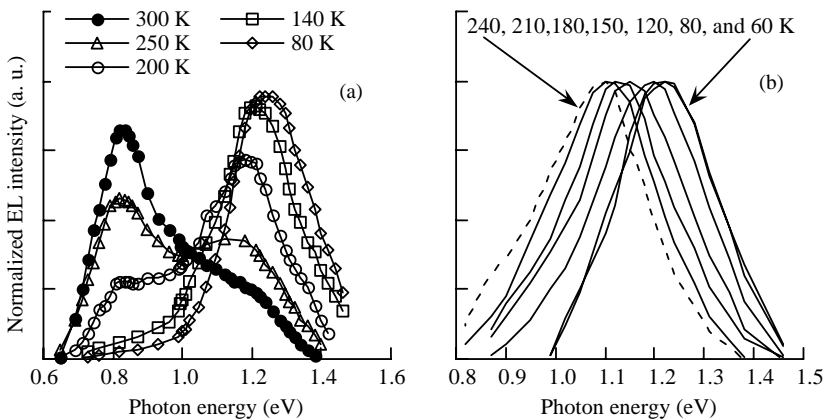


Fig. 29. EL spectrum temperature dependence from a (a) 0.2 μm , and (b) 2.0 μm a-Si:H p–i–n diode.

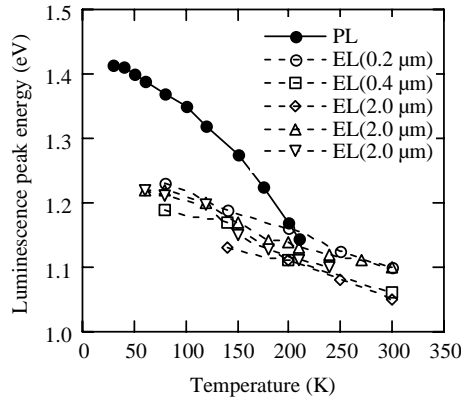


Fig. 30. Comparison of the luminescence peak energy as a function of temperature between PL_{peak} and EL_{peak} from 0.2, 0.4, and 2.0 μm p-i-n diodes.

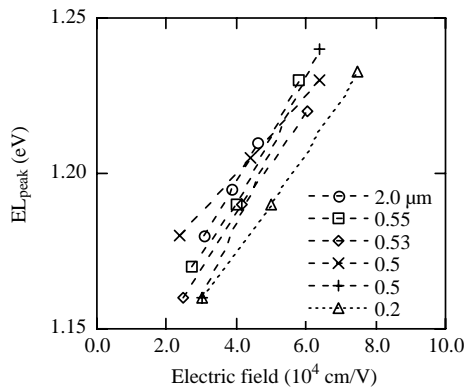


Fig. 31. EL_{peak} as a function of the electrical field for 0.2, 0.5, 0.53, 0.55 and 2.0 μm p-i-n samples at 100 K.

thermalization model similar to that in PL. The open circles in Fig. 25b indicate the favorable transition energy for the EL_{peak} . It has a much weaker temperature dependence than $E_D(T)$. Therefore, $EL_{\text{peak}}(T)$ has a weaker temperature dependence than $PL_{\text{peak}}(T)$. This is the case in Eq. (6). So both the lower EL peak energy position and its weaker temperature dependence are explained by dispersive-transport-controlled recombination.

Additional evidence of the dispersive-transport-controlled recombination is seen in the field dependence of EL_{peak} . At low temperatures the EL_{peak} shifts to a higher energy as the electrical field increases as shown in Fig. 31 for a group of p-i-n samples at 100 K. A similar shift was observed at 90 and 140 K. However, we have not observed a shift of the EL_{peak} with an increase of the electric field at $T > 200$ K. Again, the results agree with the field dependence of the carrier dispersive-transport [48]. That is, the higher the field the closer the transport level is to the mobility edge,

and the higher the transition energy for the EL peak position is in the dispersive-transport regime.

5.4. The energy profile of the defect states in *p-i-n* solar cells made with and without hydrogen dilution [8]

One problem for the PV application of a-Si:H is the effect of light-induced degradation, the so-called Staebler–Wronski effect (SWE) [50]. Several laboratories report [9,34,51] that the solar cells prepared with H-diluted reaction gas for their *i*-layers have better performance after light-soaking. One example is the discovery of two types of defects characterized as “fast” and “slow” defects according to their respective time constants for generation and annihilation deduced from solar cell degradation [51]. Yang and Chen [51] found that while “fast” and “slow” defects co-exist in solar cells made with pure silane, cells made with H-dilution appear to have predominantly “fast” defects only, resulting in much faster saturation of photodegradation. We have seen in Fig. 27 that the defect EL is relatively strong in thin diodes. In the following, we show how the EL spectra were used to characterize the defect states and their photodegradation kinetics in a-Si:H solar cells.

The top part of Fig. 32 shows the EL spectra for the pair of the *p-i_H-n* and *p-i-n* cells measured at 300 K with 0.8 V bias voltage at the initial state A. The defect band dominates. Interestingly, the defect band for the cell made with H-dilution is dominated by a single peak at ~ 0.9 eV while the cell made without H-dilution has a much more pronounced second peak at ~ 0.75 eV. To clarify the correlation of the EL defect band to the deep state energy profile, post-transit photocurrent experiments [52,53] were carried out. The transient photocurrent in the post-TOF time regime, $I(t)$, is electron-emission limited, and the energy profile of the deep

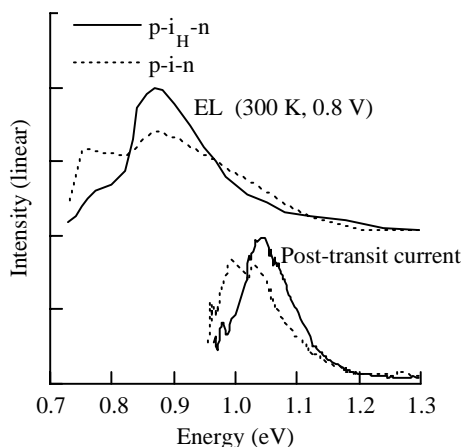


Fig. 32. The top two curves show the EL spectra in the initial state A under 0.8 V, and the bottom curves show the small-signal post-transit current results from the same *p-i_H-n* and *p-i-n* cells at room temperature.

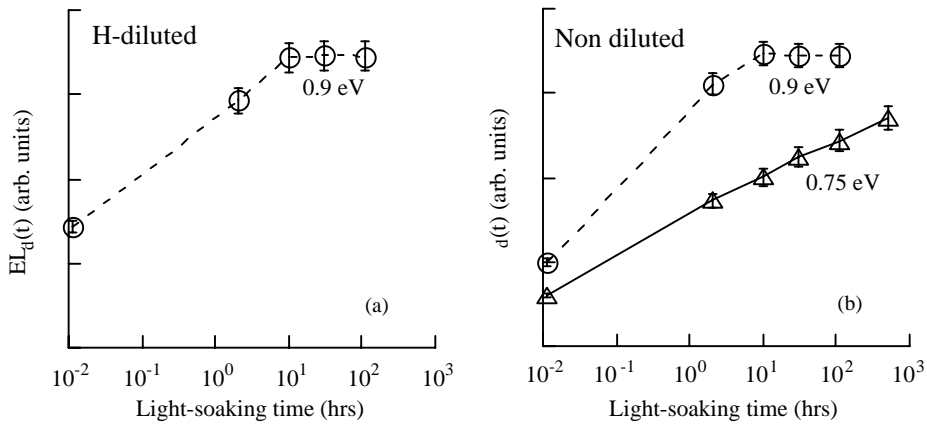


Fig. 33. EL intensities of defect components at ~ 0.9 and ~ 0.75 eV as a function of light-soaking time for (a) $p-i_n$ and (b) $p-i_n$ cell.

states (DBs), $N_d(h\nu)$, can be obtained from $I(t)t$. The lower part of Fig. 32 shows the small-signal post-transit current results from the same $p-i_n$ and $p-i_n$ cells. Regardless of the absolute value of $N_d(h\nu)$, the energy profile is obtained [8]. We have found a good correlation between the $EL_d(h\nu)$ and the $N_d(h\nu)$ profiles. The peak energy is $0.99\text{--}1.04\text{ eV}$ for the thermal transition and $0.75\text{--}0.88\text{ eV}$ for the photon emission for an optical gap of 1.7 eV . One finds that the defect relaxation energy is $0.17\text{--}0.24\text{ eV}$ compared to that of 0.1 eV found in n-type a-Si:H [1]. Comparing the results of $EL_d(h\nu)$ and $N_d(h\nu)$ in Fig. 32, we conclude that there is a single-peak band in the $p-i_n$ cell and a dual-peak band in the $p-i_n$ cell.

Since the defect band luminescence provides direct information on the defect energy profile as discussed above, we have studied the evolution of the defect properties as the material is being light-soaked. We have exposed both types of cells to 200 mW/cm^2 white light through the p-layer. The light-soaking condition used was similar to the performance photodegradation studies of the same types of solar cells. All the parameters J_F , EL/I_F and the EL spectrum were measured following step-by-step light soaking. We found slight changes in J_F and EL/I_F but clear changes in the EL defect spectra. To investigate the creation kinetics for individual components in the defect band, we have analyzed the intensities of the two peaks at ~ 0.9 and $\sim 0.75\text{ eV}$, respectively. The results are plotted in Figs. 33a and b. The intensity of the dominant peak at 0.9 eV for the $p-i_n$ cell increases first, but rapidly stabilizes after only $\sim 10\text{ h}$ of light-soaking. No significant change in the low-energy shoulder can be resolved for this type of cells. In contrast, for the non-diluted $p-i_n$ cell shown in Fig. 33b, the peak at 0.75 eV is much more pronounced and the intensity for both components increases significantly with light soaking. But while the 0.9 eV peak also stabilizes after $10\text{--}100\text{ h}$ of light soaking, the 0.75 eV peak continues to rise with no sign of saturation even beyond 1000 h of light-soaking. These observations for both types of cells are consistent with the results of the solar cell degradation studies [51] if we assume that the 0.9 and 0.75 eV peaks in the defect

Table 6

Deposition conditions and cell performances for solar cells their i-layers prepared with different H-dilution ratios (R) and thicknesses (d)

Sample	T_s (°C)	R $H_2:Si_2H_6$	d (nm)	V_{oc} (V)	J_{sc} (mA/cm ²)	FF (%)
GD288	250	20	207	0.931	11.2	71.1
GD290	250	25	215	0.926	10.3	66.2
GD299	250	50	172	0.95	9.7	71.6
GD300	250	100	170	0.948	7.4	66.3
GD289	200	25	186	0.936	9.1	72.1
GD291	200	33	189	0.944	8.9	73.0
GD292	200	50	195	0.951	9.1	71.8
GD298	200	100	153	0.971	8.1	70.3
GD293	175	33	201	0.948	8.9	73.3
GD304	175	50	156	0.985	9.7	71.1
GD294	175	100	160	0.966	6.8	71.3
GD295	150	100	159	0.972	6.4	69.6

band are associated respectively with the “fast” and “slow” defects identified from cell degradation kinetics. Thus, the EL measurements have not only confirmed the existence of the two kinetically different defect states in a-Si:H, but also provided their unique energy characteristics in the energy bandgap.

6. El and pl spectra from a-Si:H and a-SiGe:H solar cells [54]

a-SiGe:H alloy has been used as the i-layer in the narrow-gap cells. Device quality a-Si:H and a-SiGe films and their solar cells were prepared by PE-CVD on ss substrates using disilane and/or $Si_2H_6:GeH_4$ mixture made at the University of Toledo. The preparation conditions and the cell performances for H-diluted a-Si:H cells are listed in Table 6. The deposition conditions and cell performances for the a-SiGe:H cells and another group of samples made at BPSolar on glass substrates are listed in Table 7.

6.1. Comparing PL and EL spectra in a-Si:H and a-SiGe:H cells

The luminescence spectrum obtained at 80 K originates from tail-to-tail transitions. The luminescence peak roughly follows the optical band gap with a ~ 0.4 eV Stokes shift subtracted. In order to compare the EL and PL spectral lineshape, we show the normalized spectra at 80 K in Figs. 34 a and b for a group of a-Si:H cells deposited at $T_s=200^\circ\text{C}$ with increasing H dilution from $R = 25$ to 100. Interestingly, we find that the EL peak energy shifts from 1.28 to 1.43 eV and the bandwidth decreases from 294 to 206 meV as shown in Fig. 34a; whereas, the PL spectral lineshapes changed only slightly from 1.37 to 1.41 eV as shown in Fig. 34b. More interestingly, at the H dilution of $R = 100$ the EL peak energy (1.43 eV) is

Table 7
The PL and EL peak energy and the V_{oc} of a-SiGe:H solar cells

Sample ID	$\text{GeH}_4/\text{Si}_2\text{H}_6$	$V_{oc}(\text{V})$	PLpeak (eV) (at 80 K)	ELpeak (eV) (at 140 K)
Group I(UT)				
UT.GD109	Standard	0.681	1.04	0.98
GD110	(+15%)	0.634	0.98	0.96
GD111	(−15%)	0.714	1.11	1.12
GD112	H-diluted	0.813	1.16, 1.37	1.16
Group II(UT)				
L2101	50:50	0.514	1.04	1.04
L2103	45:55	0.674	1.13	1.14
L2102	40:60	0.708	1.18	1.21
Group III(BPSolar)				
A8128	a-SiGe:H	0.65	1.06	1.08
A8139	a-SiGe:H	0.63	1.01	1.07
A8226	a-Si:H	0.92	1.33	1.24

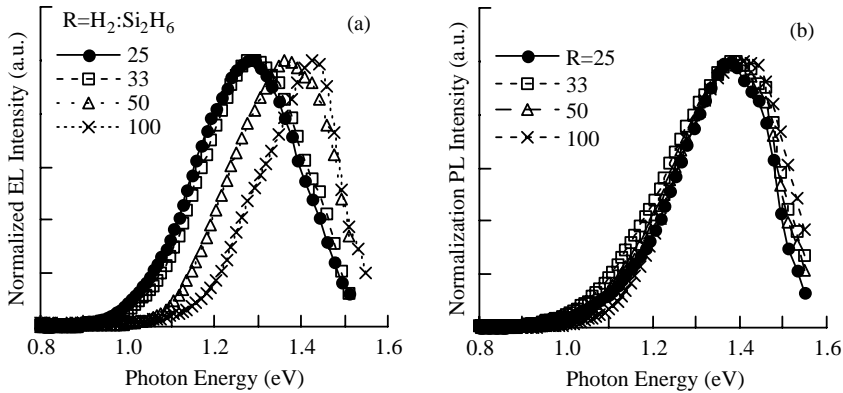


Fig. 34. Normalized luminescence spectra of (a) EL with an applied voltage of 5 V for $R = 25, 33$ and 50 cells and 6 V for $R = 100$ cell, and (b) PL for the group of a-Si:H cells deposited at $T_s=200^\circ\text{C}$ with H-dilution ratio of $R = 25, 33, 50$ and 100.

20 meV higher than the PL's (1.41 eV). To our knowledge, this phenomenon of $\text{EL}_{\text{peak}} > \text{PL}_{\text{peak}}$ has not been observed in a-Si:H based diodes. We observed the same tendency in the three groups of cells listed in Table 6; i.e. the larger peak energy shift of the EL and the higher peak energy position of EL in the $R = 100$ samples. The results cannot be due to experimental error. We will explain these using the dispersive-transport-controlled recombination model shortly.

The normalized EL and PL spectra from a pair of a-SiGe:H cells are shown in Figs. 35a and b, respectively. One may notice that some of the EL spectra were not taken at 80 K. The EL signal is too small at 80 K for high defect density a-SiGe:H cells. The data were taken with a voltage of 5 V at the temperature where the EL

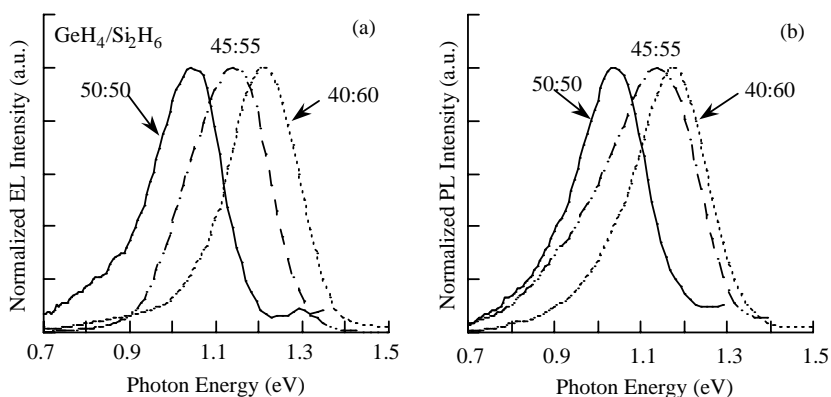


Fig. 35. Normalized luminescence spectra of (a) EL with an applied voltage of 5 V, and (b) PL for a group of a-SiGe cells with gas flow ratio of $\text{GeH}_4:\text{Si}_2\text{H}_6=45:55$, 50:50 and 40:60.

efficiency is the highest as shown in Fig. 27. The results indicate that (a) both the EL_{peak} and PL_{peak} decrease from ~ 1.2 to 1.04 eV with increasing Ge content due to the reduction of the optical gap, and (b) the EL peak energy is similar to the PL_{peak} , except that there is a low-energy shoulder on the PL spectrum for the lower Ge content sample.

6.2. Correlation between PL/EL peak energy position and V_{oc} in a-Si:H and a-SiGe:H cells

We note in Table 6 that V_{oc} is greater than 0.9 V in all the cells and it increases with an increasing H dilution ratio $R = \text{H}_2:\text{Si}_2\text{H}_6$. For the same H dilution, on the other hand, V_{oc} increases with decreasing deposition temperature, T_s . The position of the luminescence peak energy follows the same trend. In Fig. 36a we summarize the EL_{peak} and PL_{peak} data at 80 K as a function of V_{oc} for all the a-Si:H and a-SiGe cells. One can see that the higher the luminescence peak energy, the larger the V_{oc} . However, there are two interesting points as shown in Fig. 36b: First, the EL_{peak} is *not* always less than the PL_{peak} for the same sample. It can be the same or even larger as shown on the right side in Fig. 36b. Second, the EL_{peak} shifts as much as 230 meV when V_{oc} increases 47 mV; whereas, the PL_{peak} is only slightly increased by ~ 40 meV. Generally, both the luminescence peak energy and the value of the V_{oc} depend on the optical gap and the position of the quasi-Fermi level of the i-layer, so it is reasonable to observe a correlation between the luminescence peak energy and V_{oc} as shown in Fig. 36a. However, the carrier transport is not involved in PL but is in EL processes. This results in the differences between the EL_{peak} and PL_{peak} as summarized in Fig. 36b. The PL feature can be explained by the thermalization model [1]; i.e. the PL_{peak} depends on the optical gap and the carrier distribution in the band tail states as V_{oc} does. Whereas, EL is explained by the dispersive-transport-controlled recombination model [39,40] as follows.

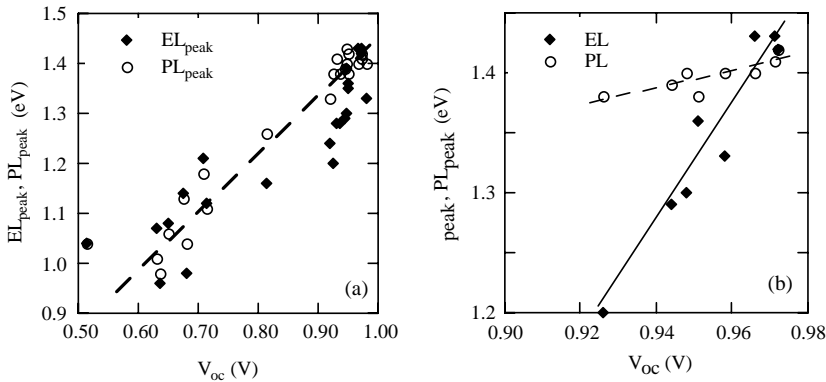


Fig. 36. Correlation between V_{oc} and the EL_{peak} (●) and PL_{peak} (○) at 80 K (a) for a-Si:H and a-SiGe cells, and (b) for a-Si:H cells with different H-dilution.

For the hydrogen-diluted cells in Fig. 34, the position of the EL_{peak} depends on the position of the transport level, E_t as shown in Fig. 25b. When the carrier lifetime is longer than its transit time, the carriers would hop down to the transport level, E_t , which is deeper than E_D , hence a lower EL_{peak} at 1.28 eV was observed compared to PL_{peak} of 1.37 eV for the cell with $R = 25$. Furthermore, the position of E_t depends on both the electric field and the carrier's lifetime (see Fig. 31). The i-layer thickness is smaller for the high H-diluted cell with $R = 100$ (see Table 6), and then the electric field across the i-layer increases (the applied voltage was 5 V for the cells with $R = 25, 33$, and 50 and 6 V for the cell with $R = 100$). Meanwhile, the carrier's lifetime decreases due to an increase in defect density. Both factors will make the E_t position shallower. It results in a larger shift of the EL_{peak} . If the energy position of E_t is higher than E_D , $EL_{peak} > PL_{peak}$ will be obtained such as in the a-Si:H cells with $R = 100$. On the other hand, for the a-SiGe:H cells in Fig. 35, the mobility lifetime product ($\mu\tau$) two or three orders of magnitude less than that for a-Si:H, so the carriers would recombine right after injection into the i-layer. When E_t is equal to E_D , $PL_{peak} \sim EL_{peak}$ as was observed in a-SiGe:H cells.

7. Nanovoid-related large red shift of PL peak energy in high-growth rate a-Si:H [4]

More recently, growth rates of a-Si:H films as high as 150 Å/s have been reached by HW-CVD [55,56]. Previous studies have shown [55,56] that the saturated defect density was below $5 \times 10^{16} \text{ cm}^{-3}$, and the Tauc optical gap did not change much; the slope of the optical absorption edge (the Urbach energy) was below 55 meV which indicates that the electronic properties of the high-growth rate films are of the same quality as the standard device-quality film. However, the microvoid volume fraction increased two orders of magnitude from the low-growth rate films ($\sim 0.01\%$) to the high-growth rate films ($\sim 1\text{--}3\%$) [56]. The growth rates and the characteristics of the

Table 8
Characteristics of a-Si:H samples with high growth rate

Sample ID	Growth rate (Å/s)	Substrate	Mass density ^a	E_{opt} (eV)	PL_{peak} at 80 K (eV)	$^1\text{H-NMR}$ very narrow line (%)	Nanovoid volume fraction ^b (%)	Raman TO mode Peak (cm^{-1})	FWHM (cm^{-1})
Standard	10	Quartz	98.0	1.68	1.36	Absence	<0.01	480	70
L388	30	Quartz			1.23		1–2	480	70
L256	50	ss			1.05		~2	480	70
L354	55	c-Si	96.0	1.65	1.10	36	~2	480	70
L353	80	c-Si	95.8	1.67	1.14	27	~2	480	70
L252	90	ss			1.12		2–3	480	70
L355	100	c-Si	95.3	1.65	1.14	24	~2	480	70
L259	110	ss			1.14		2–3	480	70
L356	115	c-Si	95.1	1.66	1.14	20	~2	480	70

^a % of c-Si density.

^b From both mass density and Ref. [56].

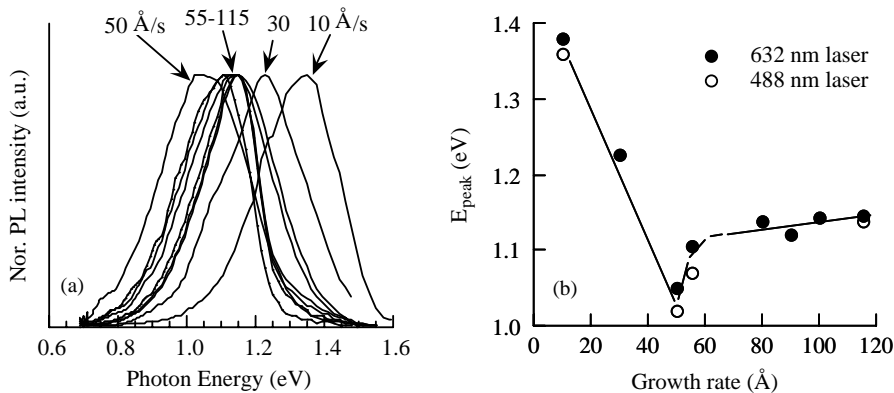


Fig. 37. (a) Normalized PL spectra excited by a 632 nm laser, (b) the PL peak energies excited by both a 632 nm (solid circles) and a 488 nm laser (open circle) at 80 K as a function of the deposition rate for HW a-Si:H films with growth rates from 10 to 115 Å/s.

a-Si:H films are listed in Table 8. A normal device-quality HW film was deposited on a rough-surface quartz substrate as a standard.

Fig. 37a shows normalized PL spectra excited by a 632 nm laser. The PL features of the standard HW-CVD film are similar to those from PE-CVD film. Surprisingly, the PL_{peak} decreases rapidly from 1.36 to 1.05 eV when the growth rate increases from 10 to 50 Å/s; it then reaches a saturated value of ~ 1.1 eV when the growth rate > 50 Å/s. The PL red shift is as large as 0.25–0.30 eV. One may question whether the excitation photon energy of the 632 nm laser is large enough for intrinsic excitation. Therefore, we also used a 488 nm laser to excite the PL. Fig. 37b plots the PL_{peak} excited by both 632 and 488 nm laser at 80 K as a function of the deposition rate.

Using the 488 nm laser, we observed PL_{peak} even 10–30 meV lower than that obtained using the 632 nm excitation. This can be understood as resulting from film non-uniformity in the growth direction and the more shallow penetration of the 488 nm laser beam into the surface [3]. The PL efficiency, on the other hand, is similar to that of the standard film in all the high-growth rate films.

In order to explore whether the PL follows carrier thermalization in band tails or not, we measured the PL temperature dependence. Fig. 38 shows normalized PL spectra excited by a 488 nm laser as a function of temperature for the film deposited at 115 Å/s (L356). The standard film PL spectra are plotted as a reference. At low temperatures, the PL main-band dominates. What we see clearly is that the PL_{peak} red shifts. As the temperature increases, the defect band gradually dominates, and the PL spectral lineshapes of the two films become similar. The data were fitted using two Gaussian functions f_1 and f_2 with linewidths of 0.20 and 0.25 eV representing the main and defect bands, respectively. Fig. 39a shows the thermal quenching of the PL

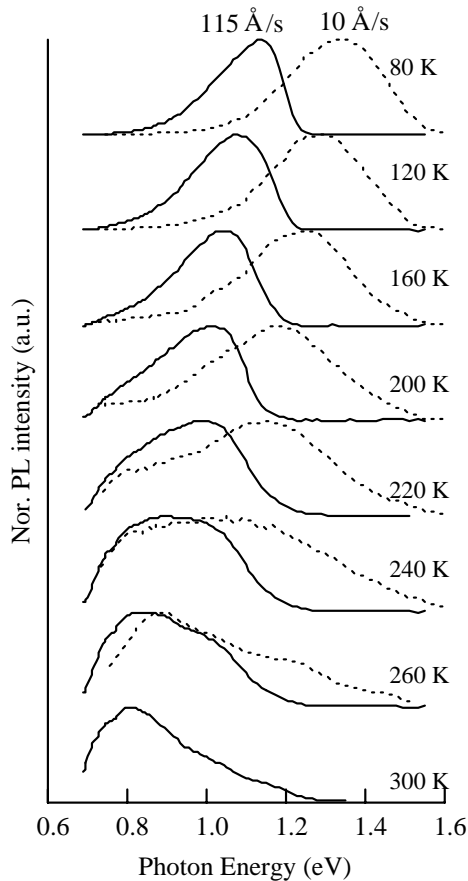


Fig. 38. Normalized PL spectra excited by a 488 nm laser as a function of temperature for two typical HW a-Si:H films with growth rates 10 Å/s (dotted lines) and 115 Å/s (solid lines).

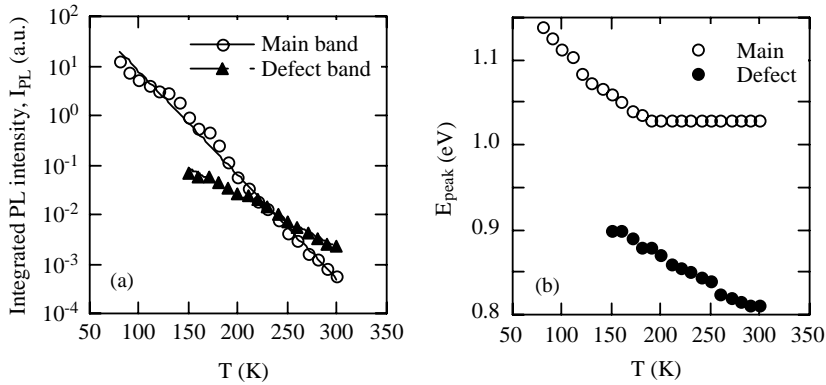


Fig. 39. The PL main band and defect band from a typical high growth rate film L356. (a) The integrated intensity and (b) the peak energy positions plotted as a function of temperature.

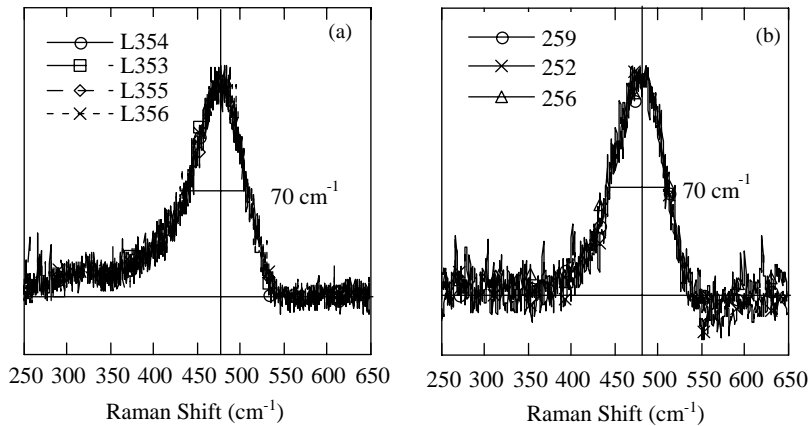


Fig. 40. Raman shift for high growth rate a-Si:H samples (a) on c-Si substrates, and (b) on ss and quartz substrates. All show the same lineshape as standard device-quality a-Si:H.

main-band intensity and a weak temperature dependence of the defect band intensity. Fig. 39b shows that the PL_{peak1} of the PL main band decreases from 1.15 to 1.04 eV as the temperature increases from 80 to 180 K and saturates at ~ 1.04 eV (where the carriers reach the bottom of the tail states). On the other hand, the peak energy position of the defect band, PL_{peak2} , decreases from 0.90 to 0.82 eV as the temperature increases from 150 to 300 K. The results in Figs. 38 and 39 indicate that both the PL intensity and the peak energy follow the model of carrier thermalization in band tail states [1]. However, the large red shift of the PL main-band (the tail-to-tail transition) is puzzling since the optical gap is similar to the standard film.

Raman spectra were used to explore how the microstructure might be related to the PL red shift. The Raman spectra in Figs. 40a and b show the same lineshapes as

standard device-quality a-Si:H; i.e. the TO mode peaks at $\sim 480\text{ cm}^{-1}$ with FWHM $\sim 70\text{ cm}^{-1}$ for all the films in Table 8. We further studied the hydrogen microstructure and the material structural ordering by ^1H -NMR and mass density measurement [57,58] on the films deposited in the same runs. We found a very narrow Lorentzian component in the spectra with $\sim 1\text{ kHz}$ linewidth in addition to the conventional Lorentzian ($\sim 3\text{ kHz}$) and Gaussian ($\sim 40\text{ kHz}$) components in the high growth rate films L353–L356. This very narrow component is related to molecular hydrogen that is absent in the standard film but comprises 20–30% of the total spectral intensity for the four samples L353–356. The mass densities were obtained by the flotation method. The average was 2.28 ± 0.02 and 2.22 ± 0.02 (g/cm^3) for the standard films and the high growth rate films, respectively. We obtain a $\sim 2\%$ volume fraction of the nanovoids in the high growth rate films. This H_2 peak exhibits a long room-temperature spin–lattice relaxation time (T_1) $\sim 1.2\text{ s}$ which implies that there is a negligible density of spin–lattice relaxation centers (i.e. dangling bonds) associated with the nanovoids. This lack of dangling bonds may indicate an ease of weak bond formation on the surfaces. Additionally, the spin–spin relaxation time (T_2) of the H_2 peak shows a dependence on the film orientation with respect to the dc magnetic field. Such unusual anisotropy in a gas system can only be understood if we consider the effects of confinement in nano-scale voids that are non-spherical and on the average aligned in the film [57,58]. The experimental NMR results of the H_2 peak fit well with the calculated properties of H_2 in an elongated elliptical geometry of 1–3 nm diameter and length several times the diameter. Meanwhile, we have learned that small-angle X-ray scattering (SAXS) also indicates that the 1–3% volume fraction nanovoids are elongated and aligned in the high growth rate films [56].

The above NMR results clarify that the nanovoids are not related to dangling bond defect centers but might be related to radiative centers. We propose that highly strained bonds (weak bonds) on the surfaces of the tube-like nanovoids result in a broad conduction band tail. In a recent molecular dynamics study of band tails in a-Si:H, Fedders and Drabold conclude that stretched bonds affect the conduction band tail; whereas, short bonds affect valence band tail states [59]. The nanovoid-related states do not produce a new type of luminescence center but only contribute to a continuous distribution of tail states. Therefore, such states cause the peak energy to red shift instead of forming a new PL peak. The temperature dependence study shown in Fig. 39b indicates that the PL peak energy saturates at $\sim 1.04\text{ eV}$ at which the carriers thermalize to the bottom of the tail states. This supports the hypothesis that the conduction band tail could be just as broad as the valence band tail. Based on the PL temperature dependence data shown in Figs. 38 and 39, these localized tail states could be exponentially distributed. For the first order approximation such as $g(E) = g_0 \exp[-(E - E_c)/E_0]$, the density difference between a narrow ($E_0 = 0.025\text{ eV}$) and a broad ($E_0 = 0.05\text{ eV}$) tail state distribution is $2.5 \times 10^{20}\text{ cm}^{-3}$ using $g_0 = 10^{22}/\text{cm}^3\text{ eV}$. The density of electronic states at the inner surface is about $2 \times 10^{20}\text{ cm}^{-3}$ for 3 nm diameter tube-like voids, and it is inversely proportional to the diameter of the voids. Since the stretched bonds affect the conduction band tail [59] one has, at least, $2 \times 10^{20}\text{ cm}^{-3}$ additional conduction tail

states in the high growth rate materials. Considering that the nearby neighbors of the void surface atoms may also contribute to the stretched bonds, the density of localized states related to the nanovoids is quantitatively consistent with a broad conduction band tail, and so are the red shift observed in the PL emission. Furthermore, the PL efficiency (which is inversely proportional to the defect density) should not decrease in the high growth rate films because the nanovoids do not create extra dangling bonds and the density of defect states is as low as in the standard device quality film [55,56]. Evidently, from our NMR studies, the long T_1 of the H_2 peak is consistent with a negligible density of spin–lattice relaxation centers (i.e. dangling bonds in a-Si:H) associated with the nanovoid surfaces. Theoretical calculation of the electronic matrix with nanovoids, experiments of transient PL spectroscopy at very low temperatures, and time of flight measurements for both conduction and valence band tails may help to further clarify the nature of the void-related electronic states. The origin of the red shift is clarified by employing 1H nuclear magnetic resonance and mass density measurements. A $\sim 2\%$ volume fraction of tube-like nanoscale voids is identified. The long spin–lattice relaxation time of H_2 in the nanovoids implies a negligible density of silicon dangling bonds on the nanovoid surfaces. We suggest that highly strained bonds on these surfaces form broad conduction band tail states that are responsible for the PL red shift.

If the Urbach absorption edge is given by the joint density of states, the broad conduction band tail should result in a broad absorption edge. The CPM results show a slightly increase of the Urbach energy [56]. We have noticed that those CPM data were not from the same group of films. Indeed, we found a 0.1 eV but not a 0.3 eV PL energy red shift when we studied the high-growth rate films deposited using a dual-filament system.

8. Summary and discussion

For the transition material from a- to μc -Si:H prepared by HW-CVD, the Raman results indicate that there is a threshold H-dilution ratio $R = 2$ at $T_s = 240$ – $250^\circ C$ and a threshold $T_s = 200^\circ C$ at $R = 3$ for the onset of the a- to μc -Si transition. The atomic and electronic structural inhomogeneity along the growth direction was shown by Raman and PL spectra with front- and back-excitation as well as with varied excitation wavelength. Both the hydrogen bonding distribution and optoelectronic properties are well correlated to the material's crystallinity due to the formation of the grain boundaries (g.b). (a) With an increase in either R or T_s , the hydrogen content, C_H , decreases in a fast and a slow regime separated by the onset of microcrystallinity. We describe that this is due to the g.b. acting as a reservoir for hydrogen, which makes the decrease of total hydrogen content slow down. The relative absorption of the 2090 cm^{-1} peak, $I_{2090}/(I_{2000} + I_{2090})$, increases with c-Si volume fraction due to the increase of SiH stretch vibration from the clustered SiH in the g.b. regions. (b) A low-energy optical absorption peaked at $\sim 1.25\text{ eV}$ and a low-energy PL band peaked at $\sim 1.0\text{ eV}$ in μc -Si:H films were observed in the transition films. The low-energy PL intensity and the peak energy decrease follow the model of

carrier thermalization in an exponential band tail [1]. We describe that there is a sub-gap formed in the g.b. regions. The absorption coefficient at 1.4 eV, $\alpha(1.4\text{ eV})$, is used to describe the DOS related to microcrystallinity. We found that the same threshold of the material's crystallinity is also visible in the increase of $\alpha(1.4\text{ eV})$, in its relevant PL (1.0 eV) band, and in the position of Fermi level. We explain that the increase of crystallinity results in an increase of the low-energy electronic density of states including both radiative and non-radiative centers.

For the transition intrinsic layer from a- to $\mu\text{c-Si:H}$ prepared by PE-CVD, we observed an enhanced low-energy PL at $\sim 1.2\text{ eV}$ in the films that show no $\mu\text{c-Si}$ features measured by XRD or Raman. Distinguished by the onset of microcrystallinity characterized by XRD, we found that there are two regimes of the PL features for the nine solar cells near transition. In the five cells below the onset of detectable microcrystallinity, the dominant factor the increase of hydrogen dilution and thickness is to improve the a-Si:H structural order. As a result, the PL peak energy is blue shifted and the linewidth is narrowed. In the four cells above the onset of microcrystallinity, the main factor is an increase of the $\mu\text{c-Si}$ volume fraction, which results in the decrease of the total PL intensity and the increase of the 1.2 eV PL band. Meanwhile, the V_{oc} quickly decreases as the PL energy is red shifted. We have shown that the PL is a sensitive tool to detect the changes of electronic structure of the localized states in relation to the sample preparation conditions.

The long-standing puzzling differences between EL and PL such as the efficiency and the peak energy position are explained not as an experimental artifact but as a direct result of the physics governing trapping and transport, the dispersive-transport-controlled carrier recombination, in amorphous materials. The critical energies are the transport level, E_t , and the demarcation energy, E_D . When E_t is equal to E_D , $\text{PL}_{\text{peak}} = \text{EL}_{\text{peak}}$. In most cases, E_t is lower than E_D . So, $\text{PL}_{\text{peak}} > \text{EL}_{\text{peak}}$ is often observed. In a thin and high defect cell, E_t can be equal or higher than E_D , then EL_{peak} equal or larger than PL_{peak} will be obtained. Comparing the thermalization-controlled geminate recombination processes of PL to the features of EL, the differences can be explained by transport-controlled non-geminate recombination in trap-rich materials.

The localized states in a pair of a-Si:H p-i-n solar cells made with and without hydrogen dilution were studied by EL spectroscopy. The slope of the EL efficiency vs. T curve was 29 K, and the defect luminescence band was dominated by a single peak at $\sim 0.9\text{ eV}$ for the cell made with H-dilution; while a slope of 37 K, and a dual-peak defect band at ~ 0.9 and $\sim 0.75\text{ eV}$ were observed for the cell made without H-dilution (see Figs. 27a and b and 32). We explain that the energy distribution of the localized states, including both the tail- and deep states, has been modified by H-dilution. The photo-degradation kinetics of the defect band suggests that the two distinctive defect states in the EL spectra are actually those identified independently as “fast” and “slow” defects (see Fig. 33), respectively, from photo-degradation studies of solar cells prepared under the same conditions. Our results indicate that not only the total density but also the energy distribution of the defects are crucial in determining the photoelectronic properties including the stability of amorphous silicon based materials.

We have summarized the correlation between the luminescence peak energy and V_{oc} . Both the luminescence peak energy and the V_{oc} are to the optical gap and the position of the quasi-Fermi level of the i-layer [60]. So, it is reasonable that one observes a correlation between the luminescence peak energy, PL_{peak} and V_{oc} . For a device quality intrinsic a-Si:H layer with an optical gap of 1.7 eV, the PL_{peak} is ~ 1.4 eV at 80 K and about 1.1 eV at room temperature. The latter is roughly the upper limit of V_{oc} . In general, V_{oc} increases slightly with increasing H-dilution before the phase transition due to improved structural ordering of the a-Si:H matrix. V_{oc} decreases rapidly with an increase of the microcrystallinity correlated to the decrease of the average optical gap and the increase defect density. At the same time, both the PL efficiency and the peak energy position decreases.

We have observed a ~ 0.3 eV red shift of PL peak energy in a-Si:H with high-growth rate ≥ 50 Å/s. A $\sim 2\%$ volume fraction of tube-like nanoscale voids is identified. The long spin–lattice relaxation time of H_2 in the nanovoids implies a negligible density of silicon dangling bonds on the nanovoid surfaces. We suggest that highly strained bonds on these surfaces form broad conduction band tail states that are responsible for the PL red shift.

Finally, we were able to measure the lattice relaxation energy in some samples. We have measured the optical absorption and the PL emission for the states that characterize the μ c-Si:H (see Figs. 8, 10 and 12.). The former is at ~ 1.25 eV and the latter is at ~ 0.9 – 1.0 eV. The energy difference between absorption and emission is ~ 0.3 eV for the g.b. states. On the other hand, for the defect states of p–i–n and p–i_H–n solar cells made at BPSolar, relaxation energy of ~ 0.2 eV was found (Fig. 32).

Acknowledgements

This work is supported by the National Renewable Energy Laboratory (NREL) Thin Film Partnership Program under subcontract ADJ-1-30630-09. We acknowledge the National Thin Film a-Si PV Team members with the sample depositions, IR measurements and for their help in discussions. The CPM measurements were supported by the NSF-INT-9802430 contract and done in H. Habuchi's lab, Gifu National College of Technology, Japan.

The authors are grateful to H. Fritzsche and S. Guha for giving us the opportunity to contribute to this issue in recognition of S. R. Ovshinsky's lifelong achievements in the development of the field of amorphous semiconductor materials and devices.

References

- [1] R.A. Street, *Hydrogenated Amorphous Silicon*, Cambridge University Press, Cambridge, UK, 1991 (Chapters 3 and 8).
- [2] G. Yue, J.D. Lorentzen, J. Lin, Q. Wang, D. Han, *Appl. Phys. Lett.* 75 (1999) 492–494; G. Yue, L.E. McNeil, D. Han, Q. Wang, *J. Appl. Phys.* 88 (2000) 4940.

- [3] D. Han, G. Yue, J.D. Lorentzen, J. Lin, H. Habuchi, Q. Wang, *J. Appl. Phys.* 87 (2000) 1882.
- [4] D. Han, G. Yue, K. Wang, J. Baugh, Y.Q. Wu, Y. Xu, Q. Wang, *Appl. Phys. Lett.* 80 (2002) 40.
- [5] D. Monroe, *Phys. Rev. Lett.* 54 (1985) 146.
- [6] T. Tiejie, A. Rose, *Solid State Commun.* 37 (1980) 49.
- [7] J. Orenstein, M. Kastner, *Phys. Rev. Lett.* 46 (1981) 1421.
- [8] D. Han, K. Wang, L. Yang, *J. Appl. Phys.* 80 (1996) 2475.
- [9] S. Guha, J. Yang, D.L. Williamson, Y. Lubianiker, J.D. Cohen, A.H. Mahan, *Appl. Phys. Lett.* 74 (1999) 1860.
- [10] J.K. Kim, J.Y. Lee, K.S. Nam, *J. Appl. Phys.* 77 (1995) 95.
- [11] J. Yang, B. Yan, J. Smeets, S. Guha, *Mater. Res. Soc. Symp. Proc.* 664 (2001) A11.3.
- [12] S.J. Jones, R. Crucet, R. Capangpangan, M. Izu, A. Banerjee, *Mater. Res. Soc. Symp. Proc.* 664 (2001) A15.1.
- [13] A.H. Mahan, J. Carapella, B.P. Nelson, R.S. Crandall, I. Balberg, *J. Appl. Phys.* 69 (1991) 6728.
- [14] U. Kroll, J. Meier, A. Shah, S. Mikhailov, J. Weber, *J. Appl. Phys.* 80 (1996) 4971.
- [15] A.H. Mahan, J. Yang, S. Guha, D.L. Williamson, *Phys. Rev. B* 61 (2000) 1677.
- [16] A.A. Langford, M.L. Fleet, B.P. Nelson, W.A. Lanford, N. Maley, *Phys. Rev. B* 45 (1992) 13367.
- [17] G.D. Cody, in: J.I. Pankove (Ed.), *Semiconductors and Semimetals*, Vol. 21 Part B, Hydrogenated Amorphous Silicon, Academic Press, New York, 1984, pp. 63.
- [18] M. Cardona, *Phys. Stat. Sol. B* 118 (1983) 463.
- [19] W. Beyer, in: N. Nickel (Ed.), *Semiconductors and Semimetals*, Vol. 61, Academic Press, San Diego, 1999, pp. 165.
- [20] G. Lucovsky, W.B. Pollard, in: J.D. Joannopoulos, G. Lucovsky (Ed.), *The Physics of Hydrogenated Silicon II*, Springer, New York, 1984, pp. 301.
- [21] T. Itoh, K. Yamamoto, K. Ushikoshi, S. Nonomura, S. Nitta, *J. Non-Cryst. Solids* 266–269 (2000) 201.
- [22] Y. Wu, J.T. Stephen, D. Han, J.M. Rutland, R.A. Crandall, H. Mahan, *Phys. Rev. Lett.* 77 (1996) 2049.
- [23] J. Baugh, D. Han, *Phys. Rev. B* 2002, in press;
J. Baugh, D. Han, *Mater. Res. Soc. Symp. Proc.* 664 (2001) A19.1.
- [24] J. Baugh, D. Han, A. Kleinhammes, Y. Wu, *Mater. Res. Soc. Symp. Proc.* 664 (2001) A27.4.
- [25] J.K. Rath, R.E.I. Schropp, *Mater. Res. Soc. Symp. Proc.* 609 (2000) A22.1.
- [26] S.S. Lee, M.J. Kong, S.F. Bent, C.M. Chiang, S.M. Gates, *J. Phys. Chem.* 100 (1996) 20015.
- [27] I.M.M. Ferreira, R.F.P. Martins, A.M.F. Cabrita, E.M.C. Fortunato, P. Vilarinho, *Mater. Res. Soc. Symp. Proc.* 609 (2000) A22.4.
- [28] D. Han, J. Baugh, G. Yue, Q. Wang, *Phys. Rev. B* 62 (2000) 7169.
- [29] S. Veprek, F.A. Sarott, Z. Iqbal, *Phys. Rev. B* 36 (1987) 3344.
- [30] P.K. Bhat, G. Diprose, T.M. Searle, I.G. Austin, P.G. LeComber, W.E. Spear, *Physica* 117B & 118B (1983) 917.
- [31] A.U. Savchouk, S. Ostapenko, G. Nowak, J. Lagowski, L. Jastrzebski, *Appl. Phys. Lett.* 67 (1995) 82.
- [32] J. Werner, M. Peisl, *Phys. Rev. B* 31 (1985) 6881.
- [33] S. Komuro, Y. Aoyagi, Y. Segawa, S. Namba, *J. Appl. Phys.* 56 (1984) 1658;
P.K. Bhat, I.G. Austin, T.M. Searle, *J. Non-Cryst. Solids* 59 & 60 (1983) 381.
- [34] D.V. Tsu, B.S. Chao, S.R. Ovshinsky, S. Guha, J. Yang, *Appl. Phys. Lett.* 71 (1997) 1317.
- [35] D.L. Williamson, *Mater. Res. Soc. Symp. Proc.* 557 (1999) 251.
- [36] G. Yue, D. Han, J. Yang, S. Guha, *Amorphous Silicon Technology—2000*, *Mater. Res. Soc. Symp. Proc.* 609 (2000) A5.9.1.
- [37] J.H. Koh, Y. Lee, H. Fujiwara, C.R. Wronski, R.W. Collins, *Appl. Phys. Lett.* 73 (1998) 1526.
- [38] G. Yue, D. Han, D.L. Williamson, J. Yang, K. Lord, S. Guha, *Appl. Phys. Lett.* 77 (2000) 3185.
- [39] D. Han, K. Wang, von Roedern, *Phys. Rev. Lett.* 77 (1996) 4410.
- [40] D. Han, K. Wang, C. Yeh, L. Yang, X. Deng, B. von Roedern, *Phys. Rev. B* 55 (1997) 15619.
- [41] J.I. Pankove, D.E. Carlson, *Appl. Phys. Lett.* 29 (1976) 620.
- [42] T.S. Nashashibi, I.G. Austin, T.M. Searle, R.A. Gibson, W.E. Spear, P.G. LeComber, *Philos. Mag.* B45 (1982) 553.

- [43] T.M. Searle, M. Hopkinson, W.A. Jackson, A.J. Rhodes, G.K. Diprose, *Philos. Mag.* B63 (1991) 179.
- [44] K. Wang, D. Han, M. Kemp, M. Silver, *J. Non-Cryst. Solids* 137 & 138 (1991) 599.
- [45] R. Vanderhagen, R. Amokrane, D. Han, M. Silver, *J. Non-Cryst. Solids* 164–166 (1993) 599.
- [46] D. Han, K. Wang, M. Silver, *J. Non-Cryst. Solids* 164–166 (1993) 339.
- [47] D. Han, K. Wang, *J. Non-Cryst. Solids* 190 (1995) 74.
- [48] J.M. Marshall, R.A. Street, M.J. Thompson, *Philos. Mag.* B 54 (1986) 51.
- [49] W. Fuhs, K. Jahn, in: H. Fritzsche (Ed.), *Amorphous Silicon and Related Material*, World Scientific, Singapore, 1988, pp. 767.
- [50] D.L. Staebler, C.R. Wronski, *Appl. Phys. Lett.* 31 (1977) 292.
- [51] L. Yang, L. Chen, *Appl. Phys. Lett.* 63 (1993) 400; in: E.A. Schiff, M. Hack, A. Madan, M. Powell, A. Matsuda (Eds.), *Amorphous Silicon Technology*, Mater. Res. Soc. Symp. Proc. 336 (1994) 669.
- [52] G.F. Senhaeve, R.P. Barclay, G.J. Adriaenssens, J.M. Marshall, *Phys. Rev. B* 39 (1989) 10196.
- [53] Bryan, D. Han, G.J. Adriaenssens, *J. Appl. Phys.* 79 (1996) 3597.
- [54] G. Yue, X. Deng, G. Ganguly, D. Han, *J. Non-Cryst. Solids* 266/269 (2000) 1119.
- [55] A.H. Mahan, Y. Xu, B.P. Nelson, R.S. Crandall, J.D. Cohen, K.C. Palinginis, A.C. Gallagher, *Appl. Phys. Lett.* 78 (2001) 3788.
- [56] A.H. Mahan, Y. Xu, D.L. Williamson, W. Beyer, J.D. Perkins, M. Vaneccek, L.M. Gedvilas, B.P. Nelson, *J. Appl. Phys.* 90 (2001) 5038.
- [57] J. Baugh, D. Han, A. Kleinhammes, Y. Wu, *Appl. Phys. Lett.* 78 (2001) 466.
- [58] J. Baugh, Alfred Kleinhammes, D. Han, Q. Wang, Y. Wu, *Science* 294 (2001) 1505.
- [59] P.A. Fedders, D.A. Drabold, *Amorphous and heterogeneous silicon thin films*, Mater. Res. Soc. Symp. Proc. 557 (1999) 403.
- [60] T. Tiedje, *Appl. Phys. Lett.* 40 (1982) 627.